1 **Distinctive aerosol-cloud-precipitation interactions in marine boundary layer clouds from the**

2 **ACE-ENA and SOCRATES aircraft field campaigns**

3

4 Xiaojian Zheng[1,a], Xiquan Dong[1], Baike Xi[1], Timothy Logan[2] and Yuan Wang[3]

5

6 [1]Department of Hydrology and Atmospheric Sciences, University of Arizona, Tucson, AZ, USA

7 [2]Department of Atmospheric Sciences, Texas A&M University, College Station, TX, USA

8 [3]Department of Earth System Sciences, Stanford University, Stanford, CA, USA

9 [a]Now at: Environmental Science Division, Argonne National Laboratory, Lemont, IL, USA

10

11 **Correspondence**: Xiquan Dong (xdong@arizona.edu)

12

13 **Abstract.** The aerosol-cloud-precipitation interactions within the cloud-topped Marine Boundary Layer

14 (MBL), are being examined using aircraft in-situ measurements from Aerosol and Cloud Experiments in

15 the Eastern North Atlantic (ACE-ENA) and Southern Ocean Clouds Radiation Aerosol Transport

16 Experimental Study (SOCRATES) field campaigns. SOCRATES clouds have a larger number (148.3

17 cm^{-3}) and smaller cloud droplets (8.0 μm) compared to ACE-ENA summertime (89.4 cm^{-3} and 9.0 μm)

18 and wintertime clouds (70.6 cm^{-3} and 9.8 μm). The ACE-ENA clouds, especially in wintertime, exhibit

19 stronger drizzle formation and growth due to enhanced collision-coalescence, attributed to the relatively

20 cleaner environment and deeper cloud layer. Furthermore, the Aerosol-Cloud Interaction (ACI) indices

21 from the two aircraft field campaigns suggest distinct sensitivities, indicating the cloud microphysical

22 responses to aerosols reside in different regimes. Aerosols during ACE-ENA winter are more likely to

23 be activated into cloud droplets under sufficient water availability and strong turbulence, given the

24 aerosol-limited regime. The enriched aerosol loading during ACE-ENA summer and SOCRATES

25 generally leads to smaller cloud droplets competing for available water vapor and exhibiting a stronger

Deleted: precipitating interaction

Deleted: of

Deleted: .

Deleted: pronounced

Deleted: strong in-

Deleted: turbulence that enhances the collision-coalescence process…

Deleted: . The

Deleted: due to more larger aerosols

Deleted: vertical

Deleted: .

ACI in the water-vapor-limit regime. Notably, the precipitation susceptibilities are more pronounced during the ACE-ENA than during the SOCRATES campaigns. The in-cloud drizzle evolutions significantly alter sub-cloud cloud condensation nuclei (CCN) budgets through the coalescence-scavenging effect, and in turn, impact the ACI assessments. The results of this study can enhance the understanding and aid in future model simulation and assessment of the aerosol-cloud interaction.

1. Introduction

Marine boundary layer (MBL) clouds substantially impact the Earth's climate system (Dong and Minnis, 2022). Sustained by large-scale subsidence and cloud-top longwave radiative cooling, MBL clouds, typically located beneath the temperature inversion at the MBL top, persistently reflect the incoming solar radiation and modulate the radiative balance (Lilly, 1968; Albrecht et al., 1995; Wood et al., 2015; Dong et al., 2023). The climatic significance of MBL cloud radiative effects, which remains largely uncertain (IPCC, 2022), is closely linked to cloud microphysical properties that are substantially influenced by surrounding aerosol conditions (Chen et al., 2014; Feingold and McComiskey, 2016). Observational evidence demonstrates that cloud microphysical responses to aerosols, defined as the aerosol-cloud interaction (ACI), can be typically viewed as decreased cloud droplet effective radii (r_c) and increased number concentrations (N_c) with more aerosol intrusion under conditions of comparable cloud water content (Feingold and McComiskey, 2016). The ACIs have been extensively investigated by different observational platforms, such as aircraft (Hill et al., 2009; Diamond et al., 2018; Gupta et al., 2022), ground-based and satellite observations (Painemal et al., 2020; Zhang et al., 2022; Zheng et al., 2022a), and model simulations (Wang et al., 2020; Christensen et al., 2023) over different maritime regions like the southeast Pacific (Painemal and Zuidema, 2011), northeast Pacific (Braun et al., 2018), southeast Atlantic (Gupta et al., 2022), and eastern North Atlantic (Zheng et al., 2022a)..

74   Furthermore, more and smaller cloud droplets not only extend cloud longevity and spatial

75   coverage but also modulate the precipitation processes, reflecting the cloud adjustments to aerosol

76   disturbances (Albrecht, 1989; Bellouin et al., 2020). Precipitation, particularly in the form of drizzle, is

77   common in MBL clouds (Wood et al., 2015; Wu et al., 2020), and the turbulence forced by stratocumulus

78   cloud-top radiative cooling can increase the cloud liquid water path, and contribute to drizzle production

79   (Ghate et al., 2019, 2021). The drizzle formation and growth processes are deeply entwined with the

80   MBL aerosols and dynamics. Aerosols have been found to suppress the precipitation frequency and

81   strength by constantly buffering cloud droplet number concentrations via activation, hence increasing

82   cloud precipitation susceptibility (Feingold and Seibert, 2009; Lu et al., 2009; Sorooshian et al., 2009;

83   Duong et al., 2011). Furthermore, the assessments of precipitation susceptibility are examined to be under

84   the influences of methodology (Terai et al., 2012), cloud morphology (Sorooshian et al., 2009; Jung et

85   al., 2016), ambient aerosol concentrations (Duong et al., 2011; Jung et al., 2016; Gupta et al., 2022), and

86   cloud thickness (Terai et al., 2012; Jung et al., 2016; Gupta et al., 2022). The in-cloud turbulence and

87   wind shear can effectively enhance collision-coalescence efficiency, stimulating drizzle formation and

88   growth, and consequently leading to enhanced precipitation (Chen et al., 2011; Wu et al., 2017). Cloud-

89   top entrainment of dryer and warmer air can potentially deplete small cloud droplets and shrink large

90   droplets via evaporation, thereby impacting cloud top microphysical processes depending on the

91   homogeneous or inhomogeneous mixing regimes (Lehmann et al., 2009; Jia et al., 2019).

92   Conversely, precipitation has been shown to exert a substantial influence on the MBL aerosol and

93   cloud condensation nuclei (CCN) budget through the coalescence-scavenging effect. The coalescence-

94   scavenging refers to the process in which cloud or drizzle droplets, containing aerosol particles, merge

95   with each other. Upon the collision-coalescence of cloud droplets, the dissolved aerosol masses within

96   the cloud droplets also collide and merge into a larger aerosol core, leading to larger aerosol particles

97   upon droplet evaporation. The sub-cloud aerosols are then replenished into the cloud layer, experiencing

98   growth within the cloud through cloud and drizzle droplet collision-coalescence, and subsequently falling

Deleted: Since precipitation is common in MBL clouds

Deleted: of drizzle drops

Deleted: turbulence. On the one hand, aerosols

Deleted: Lu et al., 2009; Sorooshian et al., 2009; Duong et al., 2011). On the other hand,

Deleted: induce

Deleted: , via

Deleted: As the

Deleted: drops descend, they are enlarged by collecting more cloud droplets …

Deleted: . However

110 and evaporating outside the cloud again. Eventually, the residual aerosols undergoing this cloud-

111 processing cycle will gradually decrease in number concentration and increase in size (Flossmann et al.,

112 1985; Feingold et al., 1996; Hudson and Noble, 2020; Hoffmann and Feingold, 2023). In addition, the

113 drizzle drops, once falling out of the cloud base, can result in net reductions in sub-cloud aerosols and

114 CCN budgets also via the precipitation scavenging processes (Wood, 2006; Zheng et al., 2022b).

115 Quantitative estimates of these effects remain ambiguous and inconclusive, which are subject to multiple

116 factors such as aerosol physicochemical characteristics, cloud morphology, and MBL dynamics and

117 thermodynamics conditions (Sorooshian et al., 2009; Duong et al., 2011; Diamond et al., 2018; Brunke

118 et al., 2022). Thus, more studies on the aforementioned processes regarding MBL aerosols and clouds

119 over different maritime regions are warranted to pursue an in-depth understanding of aerosol-cloud-

120 precipitation interactions (ACPIs).

121   The Eastern North Atlantic (ENA) stands as a desirable region for exploring MBL clouds in the

122 mid-latitude, with Graciosa Island in the Azores (39.09°N, 28.03°W) representing a focal point for such

123 studies. Located between the mid-latitude and subtropical climate zones, Graciosa is subject to the

124 meteorological influence of both the Icelandic Low and the Azores High, and the influence of aerosols

125 ranging from pristine marine air masses to those heavily influenced by continental emissions from North

126 America and Northern Europe (Logan et al., 2014; Wood et al., 2015; Wang et al., 2020). Addressing

127 the need for sustained research into the MBL clouds, the recent Aerosol and Cloud Experiments in the

128 Eastern North Atlantic (ACE-ENA) aircraft campaign (J. Wang et al., 2022) were conducted in the

129 summer (June and July) 2017 (ACEENA Sum) and winter (January and February) 2018 (ACEENA Win).

130 During these two intensive operation periods (IOPs) of ACE-ENA, the research aircraft accrued abundant

131 in-situ measurements of aerosols, clouds, and drizzle properties, providing invaluable resources for

132 studying the ACI and ACPI processes. During the summer, the Azores is located at the eastern part of

133 the high-pressure system, while during the winter, the center of the Azores high shifts to the eastern

134 Atlantic and is primarily located directly over the Azores (Mechem et al., 2018; J. Wang et al., 2022).

Deleted: coalescence-

Deleted: effect

Deleted: is

Moved (insertion) [1]

Deleted: Wang et al., 2022) were conducted in the summer 2017 (ACEENA Sum) and winter 2018 (ACEENA Win). During these two intensive operation periods (IOPs) of ACE-ENA, the research aircraft accrued abundant in-situ measurements of aerosols, clouds, and drizzle properties, providing invaluable resources for studying the ACI and ACPI processes…

4

145 Furthermore, both summer and winter IOPs of ACE-ENA are featured with anomalous stronger high-
146 pressure systems, compared to the 20-year climatology as shown in Figure S1. This meteorological
147 pattern is favorable to the prevailing and persistent stratocumulus clouds observed during the ACE-ENA,
148 especially for the winter IOP, where the enhanced large-scale subsidence would lead to a deeper
149 stratocumulus-topped MBL (Rémillard and Tselioudis, 2015; Jensen et al., 2021). The ACE-ENA
150 summer IOP is characterized by anomalously low MBL heights and substantial MBL decoupling (Miller
151 et al., 2021; J. Wang et al., 2022), while the winter IOP is featured with prevalent precipitation-generated
152 cold pools, where evaporative cooling alters the thermodynamical structure of the MBL, sustains and
153 enhances turbulence mixing, hence contributes to dynamical perturbations that can influence the behavior
154 of the MBL (Terai and Wood, 2013; Zuidema et al., 2017; Jenson et al., 2021; J. Wang et al., 2022).
155 Over the recent years, many observational studies, based on the ACE-ENA data, have focused on the
156 seasonal contrasts of the aerosol distributions and sources (Y. Wang et al., 2021b; Zawadowicz et al.,
157 2021), the cloud and drizzle microphysics vertical distributions (Wu et al., 2020a; Zheng et al., 2022b),
158 as well as the impacts of MBL conditions on the cloud structure and morphology (Jensen et al., 2021).
159 However, they seldom analyze the comprehensive interactions between aerosol, clouds and precipitation.

160   Over the Southern Ocean (SO), the Southern Ocean Clouds Radiation Aerosol Transport
161 Experimental Study (SOCRATES) field campaign (McFarquhar et al., 2021) was conducted during the
162 austral summer (January and February 2018), which marks another valuable piece of the MBL cloud
163 research. The SO, being one of the cloudiest regions globally, is predominantly influenced by naturally
164 produced aerosols originating from oceanic sources due to its remoteness, where the anthropogenic and
165 biomass burning aerosols exert minimal influence over the region (McCoy et al., 2021; Sanchez et al.,
166 2021; Twohy et al., 2021; Zhang et al., 2023). The aerosol budget in this region is primarily shaped by
167 biological aerosols, which nucleate from the oxidation products of dimethyl sulfide (DMS) emissions, as
168 well as by sea spray aerosols. Hence, the SO provides an unparalleled natural laboratory for discerning
169 the influence of these natural aerosol emissions on the MBL clouds under a pre-industrial natural

Deleted: ,

Deleted: .

environment. The summertime SO region, particularly near the SOCRATES focus area, is characterized by more frequently closed-cell mesoscale cellular convection structures (Danker et al., 2022; Lang et al., 2022). Furthermore, the MBL clouds over the SO predominantly consist of supercooled liquid water droplets, which coexist with mixed- and ice-phase processes (Y. Wang et al., 2021a; Xi et al., 2022), while the precipitation phases are examined to be primarily dominated by liquid hydrometeors (Tansey et al., 2022; Kang et al., 2024). The in-situ measurements collected from SOCRATES have cultivated numerous studies on aerosols, clouds, and precipitation over the SO using both in-situ measurements and model simulations (McCoy et al., 2020; Altas et al., 2021; D'Alessandro et al., 2021), and provides an opportunity to study the liquid cloud processes under a colder nature. As shown in Figure S1c, compositely speaking, the SOCRATES cloud cases used in this study are located ahead of the anomaly-stronger thermal ridge and behind the thermal trough, providing a set up favorable to the closed cellular MBL cloud structures (McCoy et al., 2017; Lang et al., 2022). While the region of selected SOCRATES cloud cases crosses a larger latitudinal zone and is under more consistent influence of mid-latitude cyclone systems than over the ACE-ENA region, the cloud sampling periods used in this study majority reside in the closed-cell MBL stratocumulus decks.

The cloud cases selected from the ACE-ENA and SOCRATES share similar cloud morphology (stratocumulus) while experiencing different aerosol sources and meteorological conditions. Using a synergistic approach to compare data from these different field campaigns can provide valuable insights to the community regarding the functioning physical processes of the interactions between aerosols, clouds, and precipitation under the influence of different MBL dynamic and thermodynamic conditions. This study targets the similarities and differences in the MBL aerosol, cloud, and drizzle properties, their distribution and evolution, and more appealingly, the ACIs and ACPIs between the two campaigns. The data and methods used in this study are introduced in section 2. The aerosol and CCN properties in the above- and sub-cloud regimes, as well as the vertical distributions of MBL cloud and drizzle properties, are examined in section 3. The ACI, precipitation susceptibility and drizzle impacts on the sub-cloud

aerosols and CCN (ACPI) are discussed in section 4. Finally, the findings are summarized, and the importance of this study is discussed in section 5.

2. Data and methods

2.1 Cloud and drizzle properties

The in-situ measurements of MBL cloud properties are temporally synchronized to 1 Hz resolution, corresponding to approximately 100 m (5 m) of horizontal (vertical) sampling. The sampling locations of the selected cases are indicated by the white dots in Figure S1. The Fast Cloud Droplet Probe (FCDP) onboard the aircraft during ACE-ENA can detect droplets with diameter (D_p) ranging from 1.5 μm to 50 μm, with the size bins of the probe between 1 and 3 μm (Glienke and Mei, 2020). While the SOCRATES used a similar CDP to measure droplets from 2 μm to 50 μm at a 2 μm probe size bin width. Both ACE-ENA and SOCRATES leverage the Two-Dimensional Stereo Particle Imaging Probe (2DS) to discern droplets with diameters from 5 μm to 1280 μm (Lawson et al., 2006; Glienke and Mei, 2019). The 2DS in-situ measurements will be used as additional screening to eliminate the ice particles with diameters larger than 200 μm. Moreover, the University of Washington Ice–Liquid Discriminator product, which is a Machine-learning-based single-particle phase classification of the 2DS images (Atlas et al., 2021), is used to identify small ice crystals when available. Through these three datasets, we can tease out the ice-dominated period to the utmost extent and focus on the liquid cloud processes and ACI during the SOCRATES (Wang et al., 2021).

Although these in-situ measurements can provide "ground-truth" datasets, their uncertainties must be properly analyzed and data quality must be controlled before being applied to scientific studies. The uncertainties of FCDP in sizing and concentration are approximately 30% and 20%, respectively (Baumgardner et al., 2017). Considering the significant uncertainty in the concentration of smaller particles from a photodiode probe such as 2DS (Baumgardner & Korolev, 1997; Wang et al., 2021), a diameter of 40 μm is used as the demarcation line between cloud droplets and drizzle drops (Wood et al.,

7

237 2005). Then droplet number concentrations in the overlapping size bin between FCDP and 2DS are

238 redistributed assuming a gamma distribution, thereby a complete size spectrum of cloud and drizzle can

239 be merged from FCDP and 2DS measurements. Hence, the cloud and drizzle microphysical properties

240 can be calculated.

241   The cloud droplet number concentration (N_c) is given by:

242 $N_c = \int_2^{40} n(D_p) \, dD_p,$ (1)

243 The cloud droplet effective radius (r_c, Hansen and Travis, 1974) is given by:

244 $r_c = \dfrac{\int_2^{40} r_p^3 \, n(D_p) \, dD_p}{\int_2^{40} r_p^2 \, n(D_p) \, dD_p},$ (2)

245 The cloud liquid water content (LWC_c) can be calculated by:

246 $LWC_c = \frac{4}{3} \pi \rho_w \int_2^{40} D^3 \, n(D_p) \, dD_p,$ (3)

247 where ρ_w is water density.

248 Similarly, the drizzle drop number concentration (N_d) and liquid water content (LWC_d) can be calculated

249 using the size distribution from 40 µm to 1280 µm. Particularly, the drizzle mean mass diameter (D_{mmd})

250 is given by:

251 $D_{mmd} = \left(\dfrac{\int_{40}^{1280} D_p^3 \, n(D_p) \, dD_p}{\int_{40}^{1280} n(D_p) \, dD_p} \right)^{1/3},$ (4)

252 This quantity is chosen because the D_{mmd} denotes the diameter of average mass (the third-moment

253 average) of the drizzle size distribution, which provides the link between the number concentration and

254 the mass concentration of drizzle droplets in a sample (Hinds, 1999).

255 Adapting the method in Zheng et al. (2022b), the cloud base precipitation rate (R_{CB}) is given by:

256 $R_{CB}(mm/hr) = 6\pi * 10^{-4} \int_{40\mu m}^{1280\mu m} D_{p,mm}^3 \, n(D_{p,mm}) \, U_\infty(D_{p,mm}) \, dD_{p,mm},$ (5)

257 in order to match the unit conversion, the $D_{p,mm}$ is diameter in unit of mm, $n(D_{p,mm})$ is drizzle number

258 concentration in every size bin with a unit of # m^3 mm^{-1}, and $U_\infty(D_{p,mm})$ is terminal velocity in given

259 size bin, which is calculated from the full Reynolds number theory as in Pruppacher and Klett (2010).

260 The combined threshold of $N_c > 5$ cm^{-3} and $LWC_c > 0.01$ g m^{-3} is used for determining the valid

261 cloud samples and cloud boundaries (Wood, 2005; Zheng et al., 2022b). The complete cloud vertical

262 profiles from sub-cloud to the above-cloud are selected during the ACE-ENA and SOCRATES IOPs, in

263 which the flight strategy includes sawtooth and spiral cloud transects and ramping cloud sampling. The

264 precipitation conditions are determined by whether samples of $N_d > 0.001$ cm^{-3} exists below the cloud

265 base height. In total, the selected numbers of cloud (precipitating cloud) profiles are 18 (13), 26 (13), and

266 28 (24) for ACE-ENA summer and winter IOPs along with SOCRATES, respectively. The detailed

267 selected cloud profiles are listed in Table S1, along with the cloud profile macrophysics.

268 Furthermore, the assessments of ACI are significantly impacted by the MBL dynamic and

269 thermodynamic conditions. Jones et al. (2011) suggested that the MBL would be in a well-mixed and

270 coupled condition when the difference in liquid water potential temperature (θ_L) and total water mixing

271 ratio (q_t) between the bottom of MBL and the inversion layer are less than 0.5 K and 0.5 g/kg,

272 respectively. In this regard, since the coupled and decoupled MBL conditions coexist in the selected

273 cloud cases in this study, particularly in ACE-ENA summer, which is characterized by anomalously low

274 BL heights and substantial BL decoupling. Previous studies found that, under the decoupling condition,

275 the aerosols, CCN, and moisture sources near the surface are disconnected from the cloud layer aloft,

276 hence exerting much less effective impact on the cloud microphysics (Zheng et al., 2022a; Christensen

277 et al., 2023). Therefore, we adapt and modify the metric in Jones et al. (2011) to calculate the sub-cloud

278 coupled layer, in order to ensure the aerosols and CCN measured sub-cloud are in a well-mixed state and

279 can represent the actual interaction (or contact) with the cloud layer. In this study, the q_t and θ_L at the

280 cloud base are calculated, and then their vertical variations are examined starting from the altitude of

Deleted: Additionally, for the purposes of studying the sub-cloud aerosols that actually interact with the cloud, the sub-cloud mixed layer is determined following the threshold suggested by Jones et al. (2011). Starting from the cloud base and looking downward, the mixed layer altitude is defined as where the vertical changes in liquid water potential temperature (θ_L) and total water mixing ratio (q_t) exceed 0.5 K and 0.5 g/kg, respectively. Hence, the mixed layer thickness is defined as the difference in cloud top altitude and mixed layer altitude. An example of the mixed layer identification is shown in Figure S1. The sub-cloud aerosols are thus selected between the mixed layer altitude and cloud base in order to best represent the aerosol-cloud interactions, while the above-cloud aerosols are selected between the cloud top and 200 m above (

cloud base (z_b) and looking downward. As such, the coupled point altitude (z_{cp}) is defined as the altitude where the vertical changes in q_t and θ_L exceed 0.5 K and 0.5 g/kg, respectively. Hence, the coupled layer ($H_{cp} = z_t - z_{cp}$) is defined as the layer between the cloud top altitude (z_t) and coupled point altitude (z_{cp}), hence the selection of the aerosols and CCN within the below-cloud part of the coupled layer can be viewed as in contact with the cloud. An example of the coupled layer identification is shown in Figure S2. Therefore, the degree of MBL decoupling (D_{cp}) can be quantified as the ratio of the coupled sub-cloud MBL thickness to the sub-cloud MBL thickness, where $D_{cp} = 1 - (H_{cp} - H_c)/z_b$. As shown in Table S1, the ACE-ENA summer feature with highest degree of decoupling (averaged D_{cp}=0.504), compared to the ACE-ENA winter (D_{cp}=0.370) and SOCRATES (D_{cp}=0.277).

Moved up [1]: Wang et al.,

Deleted: 2020).

2.2 Aerosol properties

The total aerosol number concentrations (N_a) from ACE-ENA and SOCRATES are measured by the airborne Condensation Particle Counter (CPC) models 3772 and 3760A, which counts the number of aerosols with diameter (D_p) larger than 3 nm and 11 nm, respectively (Kuang and Mei, 2019; SOCRATES Low Rate Data, 2022). Additionally, the Passive Cavity Aerosol Spectrometer (PCASP) onboard the ACE-ENA aircraft is capable of sizing the aerosol with D_p ranging from 0.1 μm to 3.2 μm (Goldberger, 2020). While the ultra-high sensitivity aerosol spectrometer (UHSAS) measures the size-resolved aerosol distribution from 0.06 μm to 1.0 μm during SOCRATES (Uin, 2016). Therefore, the number concentrations of accumulation mode aerosols (N_{ACC}, 0.1 μm-1 μm) can be discerned from the PCASP and UHSAS aerosol size distributions. The Aitken mode aerosols (N_{Ait}, < 0.1 μm) from the ACE-ENA is given by the fast integrated mobility spectrometer (FIMS), which can size the aerosol down to 9 nm (Olfert et al., 2008), while the N_{Ait} from SOCRATES is limited to 0.06 μm – 0.1 μm due to the limitation of UHSAS. As for the CCN measurements, the ACE-ENA utilized the Dual-Column CCN Counter at two constant supersaturation levels of 0.15% and 0.35% (Uin and Mei, 2019), while the CCN

number concentration (N_{CCN}) during SOCRATES was measured under various supersaturation levels from 0.06% to 0.87% using a scanning CCN counter (Roberts and Nenes, 2005). In this study, N_{CCN} at 0.35% supersaturation ($N_{CCN0.35\%}$) is used to ensure a direct comparison between ACE-ENA and SOCRATES. The aerosol measurements are in the temporal resolution of 1Hz. Note that the aerosol and CCN data are quality-controlled by removing the data point where the $N_c + N_d$ greater than 5 cm^{-3} or N_d greater than 0.01 cm^{-3}, to filter out the contamination of the cloud droplets, and drizzle water splashing.

The sub-cloud aerosols and CCN are selected within the below cloud base part of the coupled layer, which is described in last section, in order to better assess the aerosol-cloud interactions. The above-cloud aerosols and CCN are selected between the cloud top and 200 m above. Note that the selection criteria of 200 m above the cloud top would inevitably induce uncertainty in the cloud top ACI assessment, depending on the vertical trend of the individual aerosol profile. Over the Southeast Atlantic, Gupta et al. (2021) conducted an analysis focusing particularly on the differing impacts when biomass burning aerosols are in contact with marine stratocumulus cloud tops, using 100 m above as the demarcation, versus when they are separated by various distances, and found that significant differences were observed in cloud microphysics, owing to different droplet evaporation and nucleation, compared to separated profiles. That result is in agreement with the modeling sensitivity study over the Eastern North Atlantic by Wang et al. (2020), who found that aerosol plumes can exert impacts on the cloud-top microphysics only when they are in close contact with the cloud layer. In most cases, the ACE-ENA feature is a rather stable or slightly decreasing profile within a couple hundred meters above the cloud top, while the long-range transports, particularly during summertime, will induce an elevated aerosol layer in higher altitudes that is not in contact with the cloud layer. While the frequent new particle formation events during SOCRATES will significantly alter the free-troposphere Aitken mode aerosol budget, they would need to further subside down to impact the cloud (McCoy et al., 2021; Zhang et al., 2023). Therefore, the 200 m criteria used in this study are in the reconciliation of getting the close-to-cloud aerosol plumes and enough sample size for statistical analysis.

11

347

348

3. Aerosol, cloud, and drizzle properties of selected cases

3.1 Aerosols and CCN in above- and sub-cloud regimes

The probability density functions (PDFs) of aerosols, CCN, and cloud microphysical properties from selected cases during the ACE-ENA and SOCRATES field campaigns are presented in Figure 1. Notably, the N_a, N_{Acc} and $N_{CCN0.35\%}$ values from the SOCRATES are the highest among the three IOPs, followed by the ACE-ENA summer and winter as illustrated in both above-cloud (Figs. 1a-1c) and sub-cloud regimes (Figs. 1d-1f). Such variations can be linked to the disparate aerosol sources in the ACE-ENA and SOCRATES regions, especially during the summer and winter seasons over the Azores.

In the SOCRATES region, according to the previous studies involving back-trajectory analyses, dominant air masses within the MBL primarily originate from the south or from the west, skirting the Antarctic coast (Zhang et al., 2023), while the air masses above the MBL follow a similar transport pathway, they can also originate from the tip of southern Africa and transport southeast along the warm conveyor belt (McCoy et al., 2021). The SOCRATES above-cloud aerosols (674.6 cm-3) are primarily constituted by the Aitken mode aerosols because the mean N_{Acc} is only 62.5 cm-3. Previously, McCoy et al. (2021) reported average values of 680.69 cm-3, 546.28 cm-3 and 465.05 cm-3 for mid-troposphere, above and below cloud for the multiple SOCRATES cases, respectively. While for the individual cases the above cloud aerosols vary from a couple hundred to over a thousand (McCoy et al., 2021; Zhang et a., 2023). These aerosols are predominantly produced from the oxidation of biogenic gases, notably the dimethyl sulfide (DMS) emitted by marine biological productivity (Sanchez et al., 2018; McCoy et al., 2020). The rising air currents in MBL transport these particles into the free troposphere (FT) with dominant aerosol population over the SO (McCoy et al., 2021; Sanchez et al., 2021). And hence, it reinforces the notion that the SO represents a pre-industrial marine environment where the influence of anthropogenic and biomass-burning aerosols is mostly negligible (McCoy et al., 2020, 2021).

Deleted: 2023).

12

373   Conversely, the ENA region experiences aerosols of varied origins, spanning maritime air masses

374   to those heavily influenced by continental emissions from North America or Northern Europe, especially

375   during the summertime (Logan et al., 2014; Wang et al., 2020). The summertime air mass back-

376   trajectories within the MBL strongly feature recirculating flow around the Azores high. During the

377   wintertime, however, the air masses predominantly originate in the FT, are transported above the MBL,

378   and are then further entrained down to the MBL by large-scale subsidence, indicating less influence from

379   continental pollution (Y. Wang et al., 2021b). During the summer ACE-ENA campaign, the MBL is

380   enriched by sulfate and carbonaceous particles (Y. Wang et al., 2021b; Zawadowicz et al., 2021). This

381   enhancement is attributed both to local generation from DMS and to the long-range transport from the

382   continental air masses, resulting in the mean N_a of 312.6 cm-3 and 301.5 cm-3 for above- and sub-cloud

383   regimes, respectively. The ACE-ENA winter exhibits the lowest aerosol and CCN concentrations,

384   predominantly sourced from local maritime influences, and coupled with reduced continental air mass

385   intrusions (Zheng et al., 2018; Y. Wang et al., 2021b).

386   Figure 1a reveals that there are more above-cloud N_a during the three IOPs than sub-cloud values,

387   especially during the SOCRATES. The higher above-cloud N_a values from the three IOPs are primarily

388   contributed by Aitken mode aerosols because their corresponding N_{Acc} values are much lower (Figs.

389   1a&b). It is interesting to note that the above-cloud $N_{CCN0.35\%}$ values exceed the N_{Acc} for all three IOPs

390   (Figs. 1b&c), implying that a significant fraction of Aitken mode aerosols can be activated to become

391   CCN, corroborating findings from earlier studies (McCoy et al., 2021; Zheng et al., 2021). For the sub-

392   cloud regime, the N_a values during SOCRATES and ACE-ENA winter are ~70-80% of their

393   corresponding above-cloud values, and the N_a during ACE-ENA summer is almost identical to its above-

394   cloud value. Notice that the sub-cloud N_{Acc} values from three IOPs are more than double of the above-

395   cloud N_{Acc} values, and most of the sub-cloud accumulation mode aerosol can be activated to become

396   CCN at SS of 0.35%. It is interesting to note that the higher $N_{CCN0.35\%}$ at sub-cloud layer during

Deleted: (Logan et al., 2014; Wang et al., 2020).

Deleted: doubled their

Deleted: them

400 SOCRATES may partially result from the cloud process on aerosols (Figs. 1e&f), which is suggested by

401 previous studies (McCoy et al., 2021; Zhang et al., 2023), and will be further discussed in Section 3.1.

402   To further investigate the above- and sub-cloud aerosol properties from three IOPs, the aerosol

403 droplet size distributions are analyzed in Figure 2. It is evident that SOCRATES aerosols have the highest

404 concentrations of Aitken mode particles ($D_p = 0.06 - 0.1$ µm, given that the < 0.06 µm is not available

405 from UHSAS) for both the above- and sub-cloud regimes. McCoy et al. (2021) and Zheng et al. (2021)

406 identified analogous origins and formations of the above-cloud Aitken mode aerosols over both the SO

407 and ENA regions and concluded that these aerosols primarily originate from the nucleation of photo-

408 oxidation products of DMS, notably H_2SO_4 and MSA, in the free troposphere (FT). The differential

409 concentrations can be ascribed to the fact that sea-surface DMS concentrations in the SO are generally

410 higher than those in the ENA region (Aumont et al., 2002; Zhang et al., 2023). Moreover, DMS emissions

411 in the ENA during summer surpass those during winter (Zawadowicz et al., 2021). For the accumulation

412 mode aerosols ($0.1 - 1$ µm), the N_{Acc} values for both above- and sub-cloud regimes during SOCRATES

413 decrease monotonically with particle size. The results in Figure 2 further support the finding that Aitken

414 mode aerosols are dominant over the SO. The N_{Acc} values during ACE-ENA show slight uplifts for the

415 small accumulation mode aerosols (< 0.3 µm), particularly for summer, reflecting the signal of potential

416 long-range transport of fine-mode aerosols (Wang et al., 2020; Y. Wang et al., 2021b). Consequently,

417 such comparison reinforces the notion that the SO represents a largely pre-industrial marine environment,

418 wherein the influence of anthropogenic and biomass-burning aerosols is minimal (McCoy et al., 2020,

419 2021; Zhang et al., 2023).

420   When contrasting the aerosol size distributions in the sub-cloud regime (Fig. 2b) with those in the

421 above-cloud regime, the influence of cloud processing on aerosols is discernibly non-trivial, particularly

422 under the cloud-topped MBL conditions examined in this study. While the FT aerosols can be further

423 entrained down and contribute to the population of Aitken mode aerosols within the MBL, the sub-cloud

aerosols can also be subject to the influence of new particle formation in the upper MBL, though arguably less effective than those within the FT (Zheng et al., 2021). Additionally, in-cloud Brownian capture can lead to a substantial reduction in Aitken mode aerosols (Hudson et al., 2015; Wyant et al., 2022), providing the rationale for the observed decrease in Aitken mode aerosols in the sub-cloud regime, especially for particles smaller than 0.07 µm. In addition, cloud chemical processing, such as the aqueous-phase condensation of sulfuric gas onto the aerosol cores inside the cloud droplets, is particularly pronounced during the transitioning of Aitken mode aerosols to accumulation mode aerosols (Hudson et al., 2015; Zhang et al., 2023).

From both above- to sub-cloud regimes, the larger Aitken mode aerosols (> 0.07 µm) can be effectively enlarged to accumulation mode aerosols through coagulation and water vapor diffusional growth (Covert et al., 1996), contributing to the elevated accumulation mode aerosol distribution and increased N_{Acc} in the sub-cloud regime. These processes are particularly evidenced by the decrease of critical supersaturations from above-cloud (between 0.35% - 0.4%) to sub-cloud (between 0.3% - 0.35%) during SOCRATES (Fig. S3) because the aerosol droplet sizes are enlarged and more readily become CCN. Furthermore, the collision-coalescence combines mixtures of large and small cloud droplets, and results in the sub-cloud aerosol residuals shifting towards the larger size, upon the droplet evaporation below the cloud (often manifested as drizzle). This partially elucidates the observed increase in the tail-end of the accumulation mode aerosol distribution for all three IOPs. The elevation in sub-cloud coarse mode aerosols observed for both ACE-ENA IOPs (as seen in Fig. 2) can be attributed both to the coalescence-enlargement process and the intrusion of sea spray aerosols (e.g., sea salt). As illustrated and analyzed based on a case study during summertime that exhibits the signal of cloud-processing aerosols (Zheng et al., 2022b), as well as the long-term aerosol physicochemical properties over the ARM-ENA ground-based observatory (Zheng et al., 2018), particularly during the winter season where the production of sea spray aerosol is prevalent.

3.2 Bulk cloud microphysical properties distribution

The PDFs of MBL cloud microphysical properties (N_c, r_c, LWC_c) derived from aircraft in-situ measurements from the three IOPs are shown in Figures 1g-1i. The mean microphysical properties for the individual cloud profiles are listed in Table S2. The results in Figure 1 have demonstrated that aerosol/CCN sources and concentrations, especially from the sub-cloud regime, play an important role in cloud droplet formation and evolution. For example, the SOCRATES has the highest sub-cloud aerosols and CCN, and subsequently feature a larger number of smaller cloud droplets, given the highest N_c (148.3 cm^{-3}) and smallest r_c (8 µm) among the three IOPs. These results have further confirmed and reassured our understanding of the aerosol first indirect effect: more aerosols induce more smaller cloud droplets (higher N_c and smaller r_c) under constrained liquid water content conditions, thus the MBL clouds reflect more incoming solar radiation (Twomey, 1977). The ACE-ENA wintertime clouds feature the fewest N_c (70.6 cm^{-3}) and largest r_c (9.8 µm), while the N_c and r_c (89.4 cm^{-3} and 9 µm) during ACE-ENA summer fall between the SOCRATES and ACE-ENA winter values. Considering the aerosol competing effect against the available water vapor, the relatively abundant aerosols in SOCRATES might account for the narrower r_c distribution, which peaks between $6 - 10$ µm. SOCRATES has a lower cloud-layer water vapor mixing ratio (figure not shown) compared to ACE-ENA because the SO region has been observed to contain less precipitable water vapor than the ENA region due to the colder sea surface temperatures (Marcovecchio et al., 2023). Therefore, the aerosol and cloud properties in Figure 1 promise further examination of different cloud microphysical responses to aerosols via the ACI process. Note that the $N_{CCN0.35\%}$ and N_c values are lower than N_c values during the ACE-ENA winter IOP, which is also confirmed in previous studies (J. Wang et al., 2022; Wang et al., 2023), which is also confirmed in previous studies (J. Wang et al., 2022; Wang et al., 2023). This interesting phenomenon can potentially be attributed to a combination of factors including lower MBL aerosol sources, stronger in-cloud coalescence-scavenging depletion of sub-cloud aerosols, and the aircraft snapshots capturing the

16

488 equilibrium states of aerosols and cloud due to enhanced aerosol activations induced by stronger updrafts

489 during the ACE-ENA winter (J. Wang et al., 2022). This thereby compels further investigation into the

490 potential impacts of precipitation on the MBL CCN budget. These aerosol-cloud-precipitation

491 interactions (ACPIs) will be discussed in Section 4.

492

493 **3.3 Vertical distributions of cloud and drizzle microphysics**

494   The vertical distributions of the cloud and drizzle microphysical properties within the cloud layer

495 from the three IOPs are shown in Figure 3. To ensure the representativeness of the vertical profiles, all

496 the in-cloud samples are vertically smoothed by using a triangular moving average method, and are

497 inverse distance weighted in every 50 m moving altitude windows. Furthermore, the altitude is then

498 normalized by $z_i = \frac{Z - Z_{base}}{Z_{top} - Z_{base}}$, where $z_i = 0$ denotes cloud base and $z_i = 1$ denotes cloud top.

499 Consistent with previous discussions on the bulk microphysics distribution, the mean N_c values from

500 SOCRATES are consistently higher than ACE-ENA summer and winter for the entire cloud layer, with

501 a slight increase ranging from the cloud base to the upper-middle part ($z_i \approx 0.85$) and then decreasing

502 toward the cloud top due to cloud-top entrainment (Fig. 3a). All r_c values from the three IOPs show a

503 near-linear increase from cloud base to top, with the smallest values observed during SOCRATES and

504 the largest values observed during ACE-ENA winter (Fig. 3b).

505   The warmer and drier air near the cloud top entrains into the cloud layer and further mixes

506 downward, often resulting in the evaporation of small cloud droplets and the shrinking of droplet sizes,

507 which oppose condensational growth (Desai et al., 2021). Decreases in both N_c and LWC_c, and the

508 reduced growth of r_c near the cloud top ($z_i > 0.85$) support signals of cloud-top entrainment mixing

509 during all three IOPs. It is interesting to note that the r_c values from SOCRATES increase monotonically

510 from cloud base to top, while the r_c values from both ACE-ENA summer and winter increase until $z_i \approx$

511 0.8 and then remain nearly constant, although all of their N_c values (at $z_i \approx 0.8$) decrease towards the

Deleted:

Deleted: representative

Deleted:

Deleted: entrained

Deleted: mixing

Deleted: results

Deleted: N_c

519 cloud top. When dry air entrainment occurs at the cloud top, some of the upper-level smaller cloud

520 droplets will evaporate, which leads to decreases in N_c (Fig. 3a). As cloud-top entrainment mixing can

521 shrink large cloud droplets via evaporation, depending on the entrainment mixing rate, the nearly

522 constant r_c values (at $z_i > 0.8$) might represent the equilibrium balance between two competing

523 processes: cloud droplet condensational and collision-coalescence growths, and the entrainment mixing

524 evaporation effects.

525 While carrying the distinct discrepancies in the mean values for all layers, the N_c and r_c from

526 ACE-ENA summer and winter clouds experienced similar vertical evolutions as the SOCRATES. The

527 increases of r_c (Δr_c) from cloud base to cloud top are 4.03 µm, 4.78 µm and 5.85 µm, with percentage

528 increases of 66%, 68% and 79%, for SOCRATES, ACE-ENA summer and winter, respectively. Even

529 though, theoretically, the condensational growth effect would be more pronounced on smaller cloud

530 droplets due to their smaller surface area (Wallace and Hobbs, 2006), SOCRATES exhibits the thickest

531 mean cloud thickness but experienced the least r_c increases among the three IOPs. This suggests that

532 high aerosol loadings are limiting the overall growth of the cloud DSD in SOCRATES clouds, while the

533 ACE-ENA winter clouds show the strongest r_c increase, in contrast. This comparison suggests different

534 cloud microphysical responses to aerosol perturbations in the three IOPs, which will be further discussed

535 in Section 4.1. The LWC_c values from the three IOPs are comparable to each other. The vertical

536 distributions of MBL cloud microphysical properties examined in this study are in good agreement with

537 the previous studies conducted on these two field campaigns (Wu et al., 2020a; Y. Wang et al., 2021a; J.

538 Wang et al., 2021; Wang et al., 2023). In addition, the cloud adiabaticity is defined as $f_{ad} =$

539 LWC_c/LWC_{ad}, where the LWC_{ad} denotes adiabatic LWC (Wu et al., 2020b). As shown in Figure S4,

540 the clouds from all three IOPs feature certain levels of sub-adiabaticity above the cloud base. Considering

541 the inter-cloud layer-mean f_{ad}, the campaign-mean f_{ad} values are 0.689±0.229, 0.542±0.143, and

542 0.490±0.207 for SOCRATES, ACE-ENA summer and winter, respectively. It has been well known that

569　cloud sub-adiabaticity is primarily induced by the in-cloud collision-coalescence and the entrainment

570　mixing processes (Hill et al., 2009; Braun et al., 2018; Gao et al., 2020; Wu et al., 2020b).

571　　　To quantitatively evaluate the impact of cloud-top entrainment mixing rate on cloud droplets, we

572　adapt the method of Albrecht et al. (2016), where the cloud-top entrainment rate (w_e) can be expressed

573　as

574　　　　$$w_e = A_\sigma * \sigma_w / R_{i\sigma} ,$$ 　　　　　　　　(6)

575　where the turbulence kinetic energy (TKE) dissipation coefficient A_σ is empirically taken as 26 as in

576　Albrecht et al. (2016), and the $R_{i\sigma}$ is the buoyancy Richardson number calculated by $(g/\theta_0) *$

577　$(\Delta\theta_v h/\sigma_w^2)$. σ_w denotes the standard deviation of vertical velocities taken near the cloud top ($z_i > 0.9$),

578　and h is the MBL height. θ_0 is the reference potential temperature and $\Delta\theta_v$ is the virtual potential

579　temperature difference across the temperature inversion layer above the cloud. Given the valid cloud top

580　virtual potential temperature and vertical velocity measurements for the selected cloud cases, the

581　averaged w_e values are 0.570±0.834 cm s^{-1}, 0.581±0.560 cm s^{-1}, and 0.960±1.127 cm s^{-1} for SOCRATES,

582　ACE-ENA summer and winter, respectively. The stronger w_e during ACE-ENA winter might be induced

583　by the generally weaker cloud-top inversions and stronger near-cloud top turbulence, compared to the

584　summertime when the ENA is dominated by the large-scale high-pressure system (Ghate et al., 2021).

585　Considering the near cloud-top proportion of cloud where the LWC_c experienced decrease, the difference

586　in LWC_c (between the cloud top value the upper-middle cloud maximum for the mean profiles) for the

587　ACE-ENA summer (-0.032 g m^{-3}) is higher than the reductions in winter (-0.018 g m^{-3}) and SOCRATES

588　(-0.009 g m^{-3}), albeit that the w_e for ACE-ENA summer is comparable to SOCRATES, and much lower

589　than ACE-ENA winter values. Within the above-cloud inversion layer, the temperature (water vapor

590　mixing ratio) differences ΔT (Δq) are 1.76 K (-1.75 g kg^{-1}), 1.54 K (-1.66 g kg^{-1}) and 1.48 K (-1.09 g kg^{-1}

591　^{1}) for SOCRATES, ACE-ENA summer and winter, respectively. Therefore, the warmer and dryer

592　entrained air can partially contribute to the greater LWC_c reduction and the lower f_{ad} (0.39) during the

Deleted:

Deleted: reduction of LWC_c

595 ACE-ENA summer than those during the ACE-ENA winter ($f_{ad} = 0.45$) and SOCRATES ($f_{ad} = 0.66$)

596 near the cloud top (Fig. S4). For the three IOPs, the N_c and LWC_c exhibited a stable trend from the cloud

597 base, followed by a noticeable decrease near the cloud top mixing zone, while the changes in r_c trend

598 were not as dramatic as the others. Such characteristics of the cloud microphysics vertical profiles

599 indicate the signal of inhomogeneous mixing, which occurs when dry and warm air mixes unevenly and

600 not rapidly with the cloud air, hence partially evaporating the cloud droplets (Lehmann et al., 2009; Lu

601 et al., 2011). The results are consistent with findings in stratocumulus clouds over multiple field

602 campaigns (Brenguier et al., 2011; Jia et al., 2019) and with the findings for selected cases during the

603 ACE-ENA (Yeom et al., 2021), and the SOCRATES (Sanchez et al., 2020). While the near-cloud r_c

604 profiles for the ACE-ENA cases exhibit more constant variation, which could be possibly attributed to

605 more effective mixing due to the stronger entrainment rate, particularly during the ACE-ENA winter,

606 eventually reaching a smaller equilibrium in terms of mean sizes.

607   Figures 3d-3f illustrate the normalized profiles of MBL drizzle microphysical properties. The N_d

608 values from the three IOPs mimic each other, which all maximize at the cloud top and then monotonically

609 decrease toward the cloud base (Fig. 3d), while their LWC_d values follow a similar trend, albeit with

610 relatively large differences (Fig. 3f). In contrast to the N_d and LWC_d trends, the D_{mmd} gradually increase

611 from cloud top to cloud base (Fig. 3e), making physical sense since the drizzle droplets are typically

612 formed near cloud top and continuously grow via collision-coalescence process while falling. The ACE-

613 ENA wintertime drizzle D_{mmd} and LWC_d are distinctively larger than those in summertime and

614 SOCRATES. It is interesting to note that near the cloud top ($z_i > 0.9$), the ACE-ENA winter has

615 comparable N_d but much larger D_{mmd} than the other two IOPs, suggesting that there were more large

616 drizzle embryos formed from large cloud droplets (Fig. 3b) during ACE-ENA winter. It is noteworthy

617 that the D_{mmd} in the lower-half region of the ACE-ENA winter clouds experienced rapid growth from

Deleted:

Deleted: N_d
Deleted: LWC_d

Moved (insertion) [2]

621 ~80 μm to ~105 μm (Fig. 3e), and this increment of ~25 μm contributed to most of the D_{mmd} growth

622 from cloud top to cloud base (33.5 μm), indicating a stronger warm-rain process during the winter.

623 In order to further analyze the cloud-to-drizzle conversion processes, the cloud and drizzle droplet

624 size distributions (DSD) are categorized into four segments based on their relative position within the

625 cloud layer (Fig. 4): upper cloud ($z_i > 0.8$, Fig. 4a), upper-middle cloud ($0.5 \leq z_i < 0.8$, Fig. 4b), lower-

626 middle cloud ($0.2 \leq z_i < 0.5$, Fig. 4c) and lower cloud ($z_i < 0.2$, Fig. 4d). The cloud DSDs ($D_p < 40$

627 μm) from the three IOPs gradually shift towards larger sizes, moving from the lower to the upper cloud

628 regions. This is accompanied by the narrowing of the DSD ranges, as evidenced by the decline in the

629 cloud relative dispersion (ε). The relative dispersion of cloud droplets (ε) is a parameter that represents

630 the DSD and is defined as the ratio between the standard deviation and the mean radius of the distribution.

631 At the lower portion of the cloud (Fig. 4d), the relatively greater value of ε clearly represents the co-

632 existence of the newly formed small cloud droplets from recently activated CCNs and the sedimentation

633 of larger droplets from the upper sections of the cloud. In addition, the discrepancies in ε between the

634 three IOPs may be attributed to the sub-cloud aerosol differences, which essentially resided in different

635 microphysical regimes. Y. Wang et al. (2021a) stated that higher aerosol loading would lead to increased

636 ε due to the water vapor competition effect, supporting the discrepancy between SOCRATES and ACE-

637 ENA summer IOPs, which can be categorized as a water-vapor-limited regime. Meanwhile, the ACE-

638 ENA wintertime IOP exhibits characteristics of an aerosol-limited regime, in which the cloud DSDs tend

639 to be narrower than in the water-limited regime, due to enhanced droplet growth, and the ε values further

640 decrease with height via the condensational narrowing effect (J. Chen et al., 2018).

641 Notably, the cloud DSDs during ACE-ENA winter exhibit a more pronounced negative skew (to

642 the left) than those during ACE-ENA summer, which can be partially attribute to the activation of more

643 sub-cloud coarse mode aerosols to become larger cloud embryos, as demonstrated in Fig. 2. These coarse

644 mode aerosols, whether from primary production of sea spray or from the residuals of evaporated drizzle

Deleted:

Deleted: as

Deleted: the

Deleted: leads

Deleted: .

Deleted:

Deleted: possibly due

Deleted: S3.

653 drops, are more easily activated (or re-activated) into larger cloud droplets when they intrude (or
654 recirculate) into the cloud layer (Hudson and Noble, 2020; Hoffmann and Feingold, 2023). Nevertheless,
655 it is challenging to pinpoint the actual origins of coarse mode aerosols from the perspective of aircraft
656 observational snapshots, thus requiring further numerical modeling work. For the four cloud portions
657 from cloud base to cloud top, the skewness of summertime (wintertime) cloud DSDs are 0.627 (0.271),
658 0.358 (0.175), 0.098 (-0.063), and -0.362 (-0.554), respectively. Ascending within the cloud, the process
659 of water vapor condensation perpetually pushes the DSD towards larger sizes, culminating in a more
660 negatively skewed DSD. Concurrently, the cloud-top entrainment mixing plays a pivotal role in
661 minimizing ε in the upper cloud region, as elaborated by Lu et al. (2023). Note that in the upper region
662 of the cloud (Fig. 4a), the ACE-ENA winter clouds contain more cloud droplets close to 40 µm, albeit
663 the mean N_c is lower. This scenario is conducive to the formation of larger drizzle embryos compared to
664 summertime clouds, as depicted in Fig. 3e. In comparison, the SOCRATES clouds feature a pronounced
665 log-normal DSD than the ACE-ENA, as the DSDs peak at $D_p \sim 15$ µm throughout the cloud, and
666 subsequently, the lack of larger cloud droplets resulted in the smaller drizzle embryos near the cloud top.
667 As the newly formed drizzle drops descend and continuously grow through the collision-coalescence
668 process, the drizzle DSDs ($D_p > 40$ µm) are noticeably broadened. From upper to lower cloud regions,
669 the longer tails of the drizzle DSDs expand at the cost of smaller drizzle drops and cloud droplets via the
670 collision-coalescence process. The clouds observed during ACE-ENA, especially in wintertime, contain
671 more large drizzle drops ($D_p > 200$ µm) than SOCRATES, which is reflected in the distinct differences
672 in the vertical D_{mmd} as shown in Fig. 3e.

673 It has been intensively studied that in-cloud turbulence can stimulate collision-coalescence and
674 consequently enhance the drizzle evolution processes (Pinsky et al., 2007; Grabowski and Wang, 2013;
675 Wu et al., 2017; S. Chen et al., 2018). The turbulence strength is characterized by the turbulence kinetic
676 energy (TKE), which is calculated as:

Deleted:

678    $$TKE = \frac{1}{2}\left(\overline{u'^2} + \overline{v'^2} + \overline{w'^2}\right), \tag{7}$$

679   where the turbulent perturbations of vertical ($\overline{w'^2}$) and horizontal ($\overline{u'^2}$ and $\overline{v'^2}$) components are

680   calculated as the simple moving variance in a 10s window centered at the measurement time, without

681   window weighting function, using 1Hz data for all three IOPs. The w data is confined to an absolute

682   aircraft roll angle of less than 5° (Cooper et al., 2016). Given the average aircraft ground speed of ~140

683   m/s and vertical speed of ~5 m/s (Altas et al., 2020), the smallest resolved wavelength is 140 m. Hence,

684   within the 10s moving window, the ~50 m in the integral vertical range is able to resolve the eddies up

685   to ~1400 m in size, and preserve the potential of capturing the inertial subrange.

686   As shown in Figure 5, the vertical wind variances (Fig. 5b) in ACE-ENA winter (layer-mean of

687   0.244 m^2 s^{-2}) are generally higher than those in summer (0.153 m^2 s^{-2}) and SOCRATES (0.147 m^2 s^{-2}),

688   while the horizontal wind variances (Fig. 5c & d) are comparable between ACE-ENA winter and summer

689   but much higher than the SOCRATES, resulting in higher TKE during ACE-ENA. Note that the higher

690   w'^2 near cloud top corresponds to the stronger entrainment rate in wintertime ACE-ENA. Near the cloud

691   top, turbulence effectively enhances coalescence between the larger cloud droplets, primarily by

692   increasing the relative velocities between droplets (Magaritz-Ronen et al., 2016; Ghate and Cadeddu,

693   2019), and this is especially true for the vertical component w'^2 of TKE. While the horizontal turbulence

694   components, the u'^2 and v'^2 can also play a role in mixing the ambient air masses and contribute to the

695   broadening of DSD (Wu et al., 2017). The use of TKE provides an illustration that in-cloud turbulence

696   during ACE-ENA might be slightly stronger than that observed during SOCRATES. That being said, the

697   quantitative evaluation of the turbulent enhancement of collision-coalescence requires access to the eddy

698   dissipation rate, as typically used in model parameterizations (Grabowski and Wang, 2013; Wittle et al.,

699   2019). The smallest scales resolvable with the 1Hz measurement used in this study are on the order of

700   140 meters, thus capturing only the larger-scale end of the inertial subrange and larger turbulent motions.

701   Consequently, the ability to resolve smaller eddies and turbulent structures, crucial for understanding the

23

Deleted: .

Deleted:

Deleted: of TKE. Note that the values of the vertical turbulence are generally within the ranges of previous studies (Atlas et al., 2020; Ghate et al., 2021). Hence, the stronger drizzle formation in the ACE-ENA winter clouds can be attributed to the higher w'^2 (Fig. 5b) near cloud top (which also explains the stronger entrainment in winter), while the similar w'^2 correspond to the comparable N_d between the ACE-ENA summer and SOCRATES. The presence of turbulence throughout the cloud layer induces differential motions among the cloud droplets, increasing the likelihood of drizzle collecting smaller droplets and the droplets

Moved down [3]: (Brost et al., 1982; Feingold et al.,

Moved down [4]: drizzle DSD is sufficiently broadened, and the D_{mmd} is enlarged toward the cloud base.

Moved up [2]: It is noteworthy that the D_{mmd} in the lower-half region of the ACE-ENA winter clouds experienced rapid growth from ~80 µm to ~105 µm (Fig. 3e), and this increment of ~25 µm contributed to most of the D_{mmd} growth from cloud top to cloud base (33.5 µm

Moved down [5]: 1996; Magaritz et al.,

Deleted: 1996). As a result, the

Deleted: ¶

Deleted:). Such phenomena may potentially owe to the much stronger w'^2 in the low half cloud (Fig. 5b), where the sufficient updraft can slow down the descent of drizzle drops, thus recirculating them and elongating the drizzle residence time in the lower part of the cloud, effectively enhancing the collision-coalescence growth (Feingold et al.,

Deleted: 2009). In terms of the horizontal turbulence components, the u'^2 and v'^2 can

Deleted: 2017). However, the vertical turbulence is generally more directly influential to the drizzle formation and evolution (Brost et al., 1982; Nicholls, 1984; Pinsky and Khain, 1997; Ghate et al., 2021).

energy cascade within the inertial subrange, is limited by the too-coarse spatial and temporal resolutions and aliasing issues (Siebert et al., 2010; Muñoz-Esparza et al., 2018; Kim et al., 2022). Therefore, to fully resolve the spectrum of turbulence and quantitatively examine energy dissipation and mixing processes, access to higher-frequency measurements is required to capture smaller eddies within the inertial subrange (Siebert et al., 2010; Lu et al., 2011; Waclawczyk et al., 2017). Additionally, the further quantification of the entrainment-mixing mechanisms also requires high-frequency eddy dissipation and accurate examination of the mixing time scale (Lehmann et al., 2009; Lu et al., 2011) for individual profile. Though currently beyond the scope of this study, those mechanisms will be of interest for future investigations.

Drizzle formation and evolution in the ACE-ENA winter clouds are noticeably stronger than in the other two IOPs, which could be attributed to multiple factors. First, the ambient aerosols and CCN during winter are substantially fewer, featuring clean environments that promote the formation of generally larger cloud droplets due to the availability of more water content per droplet. Larger cloud droplets are more likely to collide and coalesce into drizzle drops, leading to relatively heavier precipitation (Chen et al., 2011; Duong et al., 2011; Mann et al., 2014). Furthermore, the wintertime clouds feature deeper cloud layers with mean thickness of (392.4 m) compared to the summertime clouds (336.3). In a thicker cloud layer with sufficient turbulence, the residence times of large cloud droplets and drizzle drops are elongated, and the chance of collision-coalescence growth can be effectively increased by recirculating the drizzle drops (Brost et al., 1982; Feingold et al., 1996; Magaritz et al., 2009; Ghate et al., 2021). Additionally, the prevalence of precipitation-evaporation-induced MBL cold pools, which disturb the MBL thermodynamics and contribute to turbulent mixing (Zuidema et al., 2017), during the wintertime might provide strong dynamical forcing to the warm-rain process (Jenson et al., 2021; J. Wang et al., 2022). As a result, the ACE-ENA wintertime drizzle DSD is sufficiently broadened, and the D_{mmd} is enlarged toward the cloud base. In comparison, although the SOCRATES exhibits even

764 thicker clouds (487.4 m), the drizzle processes are seemingly suppressed by the much higher ambient

765 aerosol and CCN concentrations.

766

767 **4 Aerosol-cloud-precipitation interactions (ACPIs)**

768 **4.1 Cloud microphysical responses on aerosols**

769 The impacts of different aerosol loadings on the cloud microphysical properties can be assessed

770 by the aerosol-cloud interaction (ACI) indices, which can be quantified as:

771 $ACI_N = \frac{\partial ln\,(N_c)}{\partial ln\,(N_{CCN,0.35\%})},$ (8)

772 and

773 $ACI_r = -\frac{\partial ln\,(r_c)}{\partial ln\,(N_{CCN,0.35\%})},$ (9)

774 which emphasizes the cloud microphysical responses to CCN via the relative logarithmic change of N_c

775 and r_c to the change in $N_{CCN,0.35\%}$ (Feingold et al., 2003; McComiskey et al., 2009). Physically, the ACI

776 process involves aerosols intruding into the cloud layer, activating as cloud droplets, and subsequently

777 altering cloud DSD and dispersion (Zheng et al., 2022a&b) under various water vapor availabilities.

778 Therefore, the cloud microphysical responses within the lower region of the cloud are assessed, which is

779 the first stage in which the sub-cloud CCN can directly interact with the cloud droplets. Furthermore, the

780 similarity in the vertical integral of LWC_c (as shown in Fig. 3c) provides comparable liquid water

781 between three IOPs for the assessment of newly generated cloud embryos from activated CCN because

782 the ACI_r is normally assessed under a fixed liquid water (Zheng et al., 2020).

783 Considering all the cases from three IOPs with available CCN measurements (some cases without

784 CCN measurements during SOCRATES), the N_c and r_c at the lower cloud ($z_i < 0.2$) are plotted against

785 the sub-cloud $N_{CCN,0.35\%}$ in Figure 6, and the ACI indices are calculated as $ACI_{N,CB}$ and $ACI_{r,CB}$ (CB

786 denoting the assessment near the cloud base). Note that the availability of valid sub-cloud measurements

787 inevitably limits the sample size, especially for SOCRATES, as shown in Table S2. As shown in Figure

Deleted: onto

Deleted: mean

Deleted:

Deleted: limit

25

792   6a, the $ACI_{N,CB}$ for the ACE-ENA wintertime (0.748) is higher than the summertime (0.617), indicating

793   that N_c is more sensitive to the sub-cloud $N_{CCN,0.35\%}$ during the winter. In other words, aerosols intruding

794   into the cloud layer are easily activated to become cloud droplets. The N_c sensitivity for the SOCRATES

795   cloud (0.692) lies between the two ACE-ENA IOPs. The $ACI_{N,CB}$ values from three IOPs are generally

796   higher than the ACI_N values from the layer-mean N_c against the sub-cloud $N_{CCN0.35\%}$ (not shown).

797   Previous studies have shown that the enhanced vertical turbulence (updraft velocity) can effectively

798   facilitate CCN replenishment into the cloud layer (Hu et al., 2021; Zheng et al., 2022a&b) and increase

799   the actual in-cloud supersaturation (Brunke et al., 2022), thus leading to a more efficient cloud droplet

800   formation, enhancing the $ACI_{N,CB}$. By correlating the mean TKE values with the CCN activation ratio

801   ($N_c/N_{CCN,0.35\%}$) for all individual cloud cases, the three IOPs show moderate but statistically significant

802   correlation coefficients of 0.36, 0.55, and 0.51 for ACE-ENA summer, winter, and SOCRATES,

803   respectively. This result reinforces the notion that the CCN activation fractions, particularly during the

804   wintertime ACE-ENA, are significantly correlated with in-cloud turbulence intensities. Furthermore,

805   more coarse mode aerosols during ACE-ENA winter are also favorable to the activation efficiency

806   (Dusek et al., 2006).

807   As for the r_c responses to CCN (Fig. 6b), the typical Twomey effect, where more CCN compete

808   against available water vapor and result in smaller cloud droplets, is evidenced by different cloud

809   susceptibility between the three IOPs. The SOCRATES features a higher $ACI_{r,CB}$ (0.311), suggesting

810   that an increase in $N_{CCN,0.35\%}$ can result in a significant decrease in r_c, compared to ACE-ENA summer

811   (0.206) and winter (0.263). Although the absolute range of variation for r_c during SOCRATES is smaller,

812   the slope is much deeper (Fig. 6b). Recall that the sub-cloud $N_{CCN,0.35\%}$ during SOCRATES is generally

813   higher and is constituted by more small-sized aerosols (as indicated in Fig. 2b). Consequently, after

814   activation, the lower part of the cloud exhibits a higher number of smaller cloud droplets, as shown in

815   Fig. 4d, even under the relatively less $N_{CCN,0.35\%}$ condition for SOCRATES. Therefore, as more CCN

Moved down [6]: Wang et al. (2022) on the seasonal dependency of the relationship between N_c and aerosols.

Deleted: , which agrees with the previous assessment by J.

Deleted:

Deleted:

26

821 intrudes into the cloud, the competition for water vapor among newly-activated cloud droplets becomes

822 more pronounced, given similar water availability. In contrast, the presence of larger cloud droplets near

823 the cloud base, whether activated from coarse-mode aerosols or remaining as residuals from collision-

824 coalescence, would elevate the r_c especially under the relatively more CCN condition, hence inevitably

825 dampening the $ACI_{r,CB}$ during ACE-ENA. However, a more comprehensive investigation into the cloud

826 microphysical responses to CCN intrusions under a larger range of various water supply conditions, and

827 further untangling the ACI from the meteorological influences, will require additional aircraft cases from

828 more field campaigns, for instance the VAMOS Ocean-Cloud-Atmosphere-Land Study (VOCALS), the

829 Cloud System Evolution over the Trades (CSET), the ObseRvations of CLouds above Aerosols and their

830 intEractionS (ORACLES), and the Aerosol Cloud meTeorology Interactions oVer the western ATlantic

831 Experiment (ACTIVATE). Note that the $ACI_{r,CB}$ values in Figure 6b are also larger than the results from

832 the layer-mean r_c against sub-cloud $N_{CCN,0.35\%}$, since the layer-mean microphysics is more subject to the

833 cloud droplet evolution processes such as condensational growth and collision-coalescence. The ACI

834 indices from three IOPs are in the ACI range of the previous studies in MBL clouds (Twohy et al., 2005;

835 Lu et al., 2009; Diamond et al., 2018) using aircraft in-situ measurements.

836 To investigate the ACI indices at the upper level of the cloud, the N_c and r_c at the upper cloud

837 ($z_i > 0.8$) are plotted against the above-cloud $N_{CCN,0.35\%}$ in Figure S5, and the ACI indices are calculated

838 as $ACI_{N,CT}$ and $ACI_{r,CT}$ (denoting the assessments near the cloud top). Compared to the $ACI_{N,CB}$ and

839 $ACI_{r,CB}$, the $ACI_{N,CT}$ and $ACI_{r,CT}$ are much weaker, especially for $ACI_{r,CT}$, as the near cloud top droplets

840 are too large for above-cloud aerosols to exert a significant influence on r_c (Diamond et al., 2018; Gupta

841 et al., 2022). While the weaker cloud top N_c dependence on the $N_{CCN,0.35\%}$ could be due to the legacy of

842 the sub-cloud CCN impacts on N_c being conveyed to the cloud top. This occurs because FT aerosols and

843 CCN can be entrained down to the MBL before and during the cloud process, as observed in the

844 assessment of inter-cloud cases. These weaker relationships support the notion that though the aerosols

27

848 entrained into the upper-cloud region can affect the cloud microphysics to a certain degree, the effects

849 are less pronounced than those from the sub-cloud aerosols (Diamond et al., 2018, Wang et al., 2020)

850 because the MBL cloud N_c and r_c variations are dominated by the condensational growth process,

851 collision-coalescence process, and cloud top entrainment mixing near the cloud top.

852

4.2 Precipitation susceptibility

854   The precipitation susceptibility relies on the assessment of relative responses in the precipitation

855 rate to the change in N_c (Feingold and Seibert, 2009; Sorooshian et al., 2009), which is defined as:

856 $S_o = -\frac{\partial ln\,(R_{CB})}{\partial ln\,(N_c)},$ (10)

857 where the R_{CB} is the cloud base precipitation rate calculated in section 2 (equation 5). By incorporating

858 all the cloud cases, including both precipitating and non-precipitating clouds (the R_{CB} can also be

859 calculated based on the drizzle DSD near the cloud base), the S_o accounts for the impact of cloud droplets

860 on the potential precipitation ability of the cloud (Terai et al., 2012).

861   As shown in Figure 7a, the R_{CB} values generally have a negative correlation with increased layer-

862 mean N_c for all three IOPs. The S_0 values are 0.979, 1.229, and 1.638, with the absolute values of

863 correlation coefficients being 0.33, 0.29, and 0.45 for SOCRATES, ACE-ENA summer and winter,

864 respectively. These correlation coefficient values fall within the reasonable range found in previous

865 studies on precipitation susceptibility in MBL stratus and stratocumulus clouds (Jung et al., 2016; Gupta

866 et al., 2022), and indicate statistically significant dependences of R_{CB} on N_c. Previous study by Terai et

867 al. (2012) found that the S_o values decrease with the increasing cloud thickness over the southeast Pacific,

868 and Jung et al. (2016) found that the S_o is more pronounced within the medium-deep clouds with

869 thickness ~300-400 m in the MBL stratocumulus over the eastern Pacific. While Gupta et al. (2022)

870 found that the S_o values are generally higher under low ambient N_a condition in the southeastern Atlantic

871 MBL. In this study, R_{CB} for the ACE-ENA winter is more susceptible to the layer-mean N_c than the

878 ACE-ENA summer and SOCRATES, which can be partially attributed to the existence of more large

879 drizzle drops (as shown in Fig. 4d) near the cloud base. As previously discussed, the ACE-ENA winter

880 feature with enhanced collision-coalescence and the drizzle-recirculating processes, especially under low

881 N_c conditions with more larger drizzle drops, leading to the increase of S_o values. In comparison, the

882 higher ambient aerosol and CCN concentrations during SOCRATES lead to relatively narrower drizzle

883 DSDs and may induce effective aerosol buffering effects, where the warm-rain processes in cloud are

884 already fairly suppressed, hence diminishing the sensitivity of R_{CB} to N_c (Stevens and Feingold, 2009;

885 Fan et al., 2020; Gupta et al., 2022).

886 In addition, it is well known that the R_{CB} can be parameterized or predicted via an approximate

887 relation with N_c and cloud thickness (H_c), which is usually parameterized in the form of $R_{CB} \propto c\, H_c^3\, N_c^{-1}$

888 (Lu et al., 2009). Following the same method, we derive the relationships from three IOPs in Figure 7b,

889 where the R_{CB} are positively (negatively) proportional to the H_c (N_c), with the exponential parameters in

890 the range of the typical values in the MBL clouds (Comstock et al., 2004; vanZanten et al., 2005; Lu et

891 al., 2009). The statistical R^2 values of R_{CB} against H_c (N_c) are 0.696 (0.177), 0.419 (0.212) and 0.165

892 (0.295), for the ACE-ENA summer, winter and SOCRATES, respectively, suggesting that the R_{CB} in

893 ACE-ENA clouds may be more determined by H_c, while the R_{CB} in SOCRATES cloud are more related

894 to N_c. Note that the relationship for SOCRATES in this study reveals a similar R_{CB} dependence on N_c

895 but a smaller dependence on the cloud thickness than the study by Kang et al. (2024), who concluded a

896 relationship of $R_{CB} = 1.73e^{-10}\, H_c^{3.6} N_a^{-1}$, based on the rain rate retrieved from radar and lidar

897 measurements and the aerosol concentration also from the SOCRATES. The discrepancies are possibly

898 due to the different sample selections and different methods in the R_{CB} calculation. Note that the mean

899 cloud thicknesses of the ACE-ENA summer (336.3 m), winter (392.4 m) and SOCRATES (487.4 m),

900 are within the thickness range where is found to exhibit stronger S_o (Terai et al., 2012; Jung et al., 2016;

901 Gupta et al., 2022).

920

4.3 Drizzle impacts on sub-cloud CCN and implication to ACI

Multiple studies on the MBL clouds have concluded that the in-cloud drizzle formation and evolution processes can effectively impact the sub-cloud CCN budgets via the coalescence-scavenging effect (Wood, 2006; Wood et al., 2012; Diamond et al., 2018; Zheng et al., 2022b; Zhang et al., 2023). Drizzle drops are formed and grow via the collision-coalescence process by collecting cloud droplets and small drizzle drops, resulting in the consumption of CCN (the precursor of cloud droplet), but in the meantime, the in-cloud N_c can be continuously buffered by the sub-cloud CCN replenishment. Although the sub-cloud aerosols (especially in large size) would be added if the drizzle fell and evaporated outside the cloud, the increment cannot compensate for the loss. Therefore, the net result of the whole process is usually presented as the depletion of sub-cloud CCN residuals, and such drizzle modulation on the CCN budget could be substantial in moderate-to-light drizzles or even non-precipitating clouds, depending on the collision-coalescence efficiency (Feingold et al., 1996; Wood, 2006; Kang et al., 2022).

The CCN loss rate due to the coalescence-scavenging effect can be calculated as:

$$L_{CCN} = -\frac{K H_c}{H_{cp}} * N_c * R_{CB}, \tag{11}$$

where the constant K (2.25 m^2 kg^{-1}) denotes the drizzle collection efficiency (Wood et al., 2006; Diamond et al., 2018). H_c is cloud thickness, and H_{cp} is the thickness of the coupled layer to ensure the change in the cloud layer can be sufficiently conveyed throughout the layer. The calculated CCN loss rate for individual cases is listed in Table S2. Considering all cloud (precipitating cloud) scenarios, the mean CCN loss rates are -7.69±13.96 cm^{-3}h^{-1} (-10.45±15.56 cm^{-3}h^{-1}), -6.29±11.65 cm^{-3}h^{-1} (-12.11±14.64 cm^{-3}h^{-1}), and -4.94±7.96 cm^{-3}h^{-1} (-5.58±8.43 cm^{-3}h^{-1}) for ACE-ENA summer, winter and SOCRATES, respectively. As the results indicate, the ACE-ENA clouds experience more substantial sub-cloud CCN loss than SOCRATES, especially in wintertime precipitating clouds. Recall that the assessment of $ACI_{r,CB}$ relies on the relative changes of r_c and N_{CCN}, while the different L_{CCN} for individual cases can

Deleted: $\frac{K H_c}{H_{mix}}$

Deleted: H_{mix}

Deleted: mixed

Deleted: 3

Deleted: 3

Deleted: 3 (

Deleted: 64cm^{-3}

Deleted: 3

Deleted: 43cm^{-3}

Deleted: Indicating

Deleted: suffer

Deleted: the

Deleted: for the

957 result in the shrinking of the N_{CCN} variation ranges (imagine the abundant CCN are depleted by the

958 coalescence-scavenging). In other words, the given change in r_c corresponds to a narrowed change in

959 N_{CCN}. Mathematically speaking, the assessment of $ACI_{r,CB}$ depends on the ratio of the numerator (change

960 in r_c) and the denominator (change in N_{CCN}). Under the circumstances of substantial cloud-processing to

961 the aerosols, the altered sub-cloud CCN budgets are reflected as a smaller denominator, versus the less

962 altered numerator, hence mathematically presented as an enlarged $ACI_{r,CB}$. Therefore, the coalescence-

963 scavenging effect can not only deplete the sub-cloud CCN, but also quantitatively amplify the assessment

964 of cloud microphysics susceptibilities (Feingold et al., 1999; Duong et al., 2011; Jung et al., 2016; Zheng

965 et al., 2022b). In order to examine the potential impact of the aforementioned processes on the ACI

966 assessment, a sensitivity analysis is conducted by simply retrospecting the sub-cloud $N_{CCN0.35\%}$

967 according to their L_{CCN}. For each retrospective time step ΔT, the r_c values are held unchanged, and the

968 retrospective $N_{CCN0.35\%}$ values for individual cloud cases are given by $N_{CCN0.35\%} - L_{CCN} * \Delta T$, and then

969 the $ACI_{r,CB}$ can be recalculated. Note that assuming a constant r_c value over time inevitably induces

970 uncertainty and biases, as it does not consider the microphysical processes affecting the cloud droplet

971 mean size. However, previous numerical experiments show that the noticeable impact on the cloud mean

972 radius through collision-coalescence necessitates a high degree of CCN depletion, and the quantified

973 percentage changes in droplet mean sizes are several times less than the changes in CCN depletion

974 (Feingold et al., 1996). Hence, the retrospective method, from an observational snapshot point of view,

975 provides a direction that enables the assessment of $ACI_{r,CB}$ as if before the sub-cloud aerosols and CCN

976 are scavenged by in-cloud coalescence-scavenging and precipitation scavenging processes.

977   As shown in Figure 8, the $ACI_{r,CB}$ values tend to decrease with the retrospective time, which

978 indicates the retrospective CCN variation range is enlarged and counteracting the coalescence-

979 scavenging amplification. The detailed illustration of the different $ACI_{r,CB}$ calculated from the scattered

980 r_c and sub-cloud $N_{CCN0.35\%}$ is shown in Figure S6. Note that the $ACI_{r,CB}$ decreasing rates for the

Deleted:

Deleted: Hence

983 precipitating clouds (Fig. 8b) are not as strong as for all clouds because the non-precipitating clouds have

984 smaller L_{CCN} largely due to weaker collision-coalescence. Hence, the time retrospected might quickly

985 exceed the actual time scale of processing of cloud droplets. In other words, the time needed to store the

986 sub-cloud CCN to the budget before cloud existence is shorter. Therefore, the retrospective of the sub-

987 cloud CCN budget will yield an alternative assessment of ACI, assuming that the drizzle processes have

988 not yet significantly impacted the sub-cloud CCN budget, especially for the assessment under the

989 precipitating clouds. However, examining the exact precipitating timing is challenging since the aircraft

990 provides a snapshot of the cloud and aerosol information. Thus, this retrospective study only provides a

991 possible direction, and the result should be interpreted with caution.

992

993 **5. Summary and Conclusions**

994   Based on the aircraft in-situ measurements during ACE-ENA and SOCRATES, the vertical

995 distributions and the evolutions of the aerosol, cloud, and drizzle properties are investigated under the

996 cloud-topped MBL environments. The aerosols and CCN from SOCRATES are the highest among the

997 three IOPs, followed by ACE-ENA summer and winter in descending order in both above- and sub-cloud

998 regimes. The differences can be attributed to the differences in aerosol size distributions between ACE-

999 ENA and SOCRATES, which are largely due to the aerosol sources in those regions. The SOCRATES

1000 features the pre-industrial natural environment enriched by aerosols from marine biological productivity

1001 and without the contamination of anthropogenic aerosols, while the ACE-ENA features the aerosols from

1002 varied sources, including maritime and continental emissions, with distinct seasonal variations.

1003 Examining the aerosol size distributions in sub-cloud versus above-cloud regimes manifests the

1004 significant influence of cloud processing on aerosols. Physical processing like in-cloud Brownian capture

1005 can reduce Aitken mode aerosols, while the chemical processes transform Aitken mode aerosols to larger

1006 sizes, moving them toward the accumulation mode. In addition, the in-cloud coalescence processes shift

1007 sub-cloud aerosol residuals to larger sizes, as multiple aerosols combine into a single aerosol core inside

32

the cloud droplet during collision-coalescence, explaining the observed increase in the tail-end of the aerosol distribution for all IOPs.

As for the cloud and drizzle properties, the SOCRATES clouds feature more and smaller cloud droplets than the ACE-ENA summertime and wintertime clouds, with the r_c growths (and percentage increases), from cloud base to top, being 4.03 µm (0.66%), 4.78 µm (0.68%), and 5.85 µm (0.79%) for SOCRATES, ACE-ENA summer, and winter, respectively. The cloud-top entrainment mixing is evidenced in the observed decline of both N_c and LWC_c near the cloud top. The mean cloud-top entrainment rates (w_e) are 0.570±0.834 cm s^{-1}, 0.581±0.560 cm s^{-1}, and 0.960±1.127 cm s^{-1} for SOCRATES, ACE-ENA summer and winter, respectively. The strongest w_e during ACE-ENA winter is owing to weaker cloud-top inversions and stronger near-cloud-top turbulence. The values of the TKE for three IOPs are generally within the ranges of previous studies (Atlas et al., 2020; Ghate et al., 2021). For drizzle vertical distribution, N_d from the three IOPs all exhibit decreases from cloud top to cloud base, while D_{mmd} are in opposite directions with a maximum at the cloud base. The ACE-ENA wintertime clouds feature more prominent drizzle formation and evolution owing to the combined effects of relatively cleaner environment, deeper cloud layer, and slightly stronger in-cloud vertical turbulence, which substantially enhances the collision-coalescence and the drizzle re-circulating processes, compared to the other two IOPs. While satellite retrievals of droplet number concentration heavily rely on the adiabatic cloud assumption and are usually given as a constant of $f_{ad} = 0.8$, the in-situ observational evidence found in this study further confirms the unrealistic nature of this assumption. It will be of interest to utilize multiple aircraft measurements (campaigns) to explore the variability of MBL cloud and drizzle microphysical properties over different marine regions. This can help examine potential predictors for f_{ad}, which will aid in satellite-based retrievals and aerosol-cloud interaction assessments (Painemal and Zuidema, 2011; Grosvenor et al., 2018; Painemal et al., 2021).

1055 Comparing the seasonality of cloud base precipitation rate (R_{CB}) during ACE-ENA, more cases

1056 with large observed R_{CB} during the winter season, which is consistent with J. Wang et al. (2022). Notably,

1057 the sensitivity of R_{CB} to N_c is more pronounced for the ACE-ENA during both winter (with $S_o = 1.638$)

1058 and summer (1.229) compared to the SOCRATES ($S_o = 0.979$). This is partly due to the much higher

1059 R_{CB} induced by larger drizzle drops near the cloud base for ACE-ENA, a result of turbulence-driven in-

1060 cloud droplet interactions, especially under low N_c condition. Furthermore, R_{CB} can be approximated by

1061 a relationship involving N_c and H_c, as suggested in prior research. The relationships established in this

1062 study indicate that ACE-ENA clouds, are largely determined by H_c, while SOCRATES clouds are more

1063 influenced by the N_c. The combination of a deeper cloud layer along with relatively lower ambient

1064 aerosol concentration, which eventually lead to stronger drizzle production and evolution, during ACE-

1065 ENA, especially during the winter season, results in more robust precipitation susceptibility. Note that

1066 considering the combined factors of aerosol loadings, cloud morphology and thicknesses, and the

1067 assessment methodology, the derived S_o values in this study are generally higher (or close to the upper

1068 end) compared to previous studies (Lu et al., 2009; Duong et al., 2011; Terai et al., 2012; Jung et al.,

1069 2016; Gupta et al., 2022).

1070 The investigations of the ACI via the $ACI_{N,CB}$ and $ACI_{r,CB}$ indices reveal that during the ACE-

1071 ENA wintertime, N_c is more sensitive to changes in $N_{CCN0.35\%}$, indicating aerosols more readily activate

1072 to become cloud droplets compared to those in the summer, which is consistent with the previous

1073 assessment by J. Wang et al. (2022) on the seasonal dependency of the relationship between N_c and

1074 aerosols. One influencing factor is the strong dynamic mechanism that speeds up the infusion of CCN

1075 into the cloud layer, thus aiding droplet formation. The moderate but statistically significant correlation

1076 coefficients between the CCN activation fractions and the TKE agree with a previous study that found

1077 the local activation fraction of CCN to be strongly associated with increased updrafts (Hu et al., 2021).

1078 Furthermore, the presence of larger aerosols during ACE-ENA winter enhances the droplet activation

Deleted: Notably,

Deleted: sensitivity

Moved (insertion) [6]

Deleted: .

Deleted: vertical turbulence, which

1083   process. The SOCRATES IOP highlights a higher $ACI_{r,CB}$, indicating a pronounced decrease in r_c with

1084   increasing $N_{CCN0.35\%}$. The $ACI_{r,CB}$ in ACE-ENA is dampened by the presence of more larger cloud

1085   droplets near the cloud base, particularly under relatively higher $N_{CCN0.35\%}$. However, the combined

1086   effect of the relatively cleaner environment and sufficient water vapor results in stronger cloud

1087   microphysical responses during the ACE-ENA wintertime than in the summertime. Note that the ACI

1088   indices from this study lie in the higher end of the ACI ranges estimated via remote sensing (McComiskey

1089   et al., 2009; Dong et al., 2015; Zheng et al., 2022a) because the aircraft assessment of ACI is based on

1090   measurements where the aerosols are in direct contact with the cloud layer. Arguably, the assessment of

1091 N_c responses to $N_{CCN0.35\%}$ would inevitably be affected by the collision-coalescence process near the

1092   cloud base, where simultaneously, the CCN replenishment buffers the N_c and the collision-coalescence

1093   process depletes N_c. Hence, finding a layer where these two effects maintain a dynamic balance in N_c

1094   might aid in a more accurate assessment and more fundamental understanding of the ACI, which might

1095   be revealed by the LES or parcel model simulations.

1096   Additionally, the in-cloud drizzle formation and evolution processes significantly influence the

1097   sub-cloud CCN budgets via the coalescence-scavenging effect, which can potentially exaggerate the

1098   assessment of cloud microphysics susceptibilities. Based on the CCN loss rate (L_{CCN}) from ACE-ENA

1099   and SOCRATES, a sensitivity analysis is performed focusing on retrospectively adjusting the sub-cloud

1100   CCN according to their L_{CCN}. Results showed that this adjustment led to a decreased $ACI_{r,CB}$,

1101   highlighting the significance of the coalescence-scavenging process on the ACI assessment. However,

1102   due to the fact that aircraft only provide a snapshot of the clouds and aerosol information, determining

1103   the precise drizzle timing for the individual cloud is challenging. Hence, findings from this retrospective

1104   approach provide only a direction or theory, and should be taken cautiously. Nevertheless, pursuing

1105   further modeling experiments on this matter may be worthwhile. For example, the exact drizzling time

1106   could be pinpointed within a model using an Eulerian framework or traced using a Lagrangian framework.

Deleted: While the

Deleted: provides more connected circumstances between

Deleted: and

1110 Nevertheless, the CCN adjustment could more accurately reflect the true characteristics of the cloud and
1111 the MBL CCN budget, potentially aiding in a more precise assessment of ACI. Therefore, future works
1112 would focus on the model simulation on the MBL clouds from ACE-ENA and SOCRATES and further
1113 assess the modeled ACI under the observational constraints, as well as the continuous development of
1114 the warm rain microphysical parameterizations, in order to aid in the better represent the MBL clouds in
1115 multiple regions.

1116

1117

1123

1124 *Author contributions.* The original idea of this study is discussed by XZ, XD, and BX. XZ performed the
1125 analyses and wrote the manuscript. XZ, XD, BX, TL, and YW participated in further scientific
1126 discussions and provided substantial comments and edits on the paper.

1127

1130

References.

Albrecht B. A.: Aerosols, Cloud Microphysics, and Fractional Cloudiness, Science, 245, 1227-1230, 10.1126/science.245.4923.1227, 1989

Albrecht, B. A., Bretherton, C. S., Johnson, D., Scubert, W. H., and Frisch, A. S.: The Atlantic Stratocumulus Transition Experiment—ASTEX, B. Am. Meteorol. Soc., 76, 889-904, 10.1175/1520-0477(1995)076<0889:Taste>2.0.Co;2, 1995.

Albrecht, B., Fang, M., and Ghate, V.: Exploring Stratocumulus Cloud-Top Entrainment Processes and Parameterizations by Using Doppler Cloud Radar Observations, J. Atmos. Sci., 73, 729-742, 10.1175/JAS-D-15-0147.1, 2016.

Atlas, R. L., Bretherton, C. S., Blossey, P. N., Gettelman, A., Bardeen, C., Lin, P., and Ming, Y.: How Well Do Large-Eddy Simulations and Global Climate Models Represent Observed Boundary Layer Structures and Low Clouds Over the Summertime Southern Ocean?, Journal of Advances in Modeling Earth Systems, 12, e2020MS002205, https://doi.org/10.1029/2020MS002205, 2020.

Atlas, R., Mohrmann, J., Finlon, J., Lu, J., Hsiao, I., Wood, R., and Diao, M.: The University of Washington Ice–Liquid Discriminator (UWILD) improves single-particle phase classifications of hydrometeors within Southern Ocean clouds using machine learning, Atmos. Meas. Tech., 14, 7079-7101, 10.5194/amt-14-7079-2021, 2021.

Baumgardner, D. and Korolev, A.: Airspeed Corrections for Optical Array Probe Sample Volumes, J. Atmos. Ocean. Tech., 14, 1224-1229, https://doi.org/10.1175/1520-0426(1997)014<1224:ACFOAP>2.0.CO;2, 1997.

Baumgardner, D., Abel, S. J., Axisa, D., Cotton, R., Crosier, J., Field, P., Gurganus, C., Heymsfield, A., Korolev, A., Krämer, M., Lawson, P., McFarquhar, G., Ulanowski, Z., and Um, J.: Cloud Ice Properties: In Situ Measurement Challenges, Meteor. Monogr., 58, 9.1-9.23, https://doi.org/10.1175/AMSMONOGRAPHS-D-16-0011.1, 2017.

Braun, R. A., Dadashazar, H., MacDonald, A. B., Crosbie, E., Jonsson, H. H., Woods, R. K., Flagan, R. C., Seinfeld, J. H., and Sorooshian, A.: Cloud Adiabaticity and Its Relationship to Marine Stratocumulus Characteristics Over the Northeast Pacific Ocean, J. Geophys. Res.-Atmos., 123, 13790 - 13806, 10.1029/2018jd029287, 2018.

Brenguier, J. L., Burnet, F., and Geoffroy, O.: Cloud optical thickness and liquid water path – does the k coefficient vary with droplet concentration?, Atmos. Chem. Phys., 11, 9771-9786, 10.5194/acp-11-9771-2011, 2011.

Brost, R. A., Wyngaard, J. C., and Lenschow, D. H.: Marine Stratocumulus Layers. Part II: Turbulence Budgets, J. Atmos. Sci., 39, 818-836, 10.1175/1520-0469(1982)039<0818:MSLPIT>2.0.CO;2, 1982.

Brunke, M. A., Cutler, L., Urzua, R. D., Corral, A. F., Crosbie, E., Hair, J., Hostetler, C., Kirschler, S., Larson, V., Li, X.-Y., Ma, P.-L., Minke, A., Moore, R., Robinson, C. E., Scarino, A. J., Schlosser, J., Shook, M., Sorooshian, A., Lee Thornhill, K., Voigt, C., Wan, H., Wang, H., Winstead, E., Zeng, X., Zhang, S., and Ziemba, L. D.: Aircraft Observations of Turbulence in Cloudy and Cloud-Free Boundary Layers Over the Western North Atlantic Ocean From ACTIVATE and Implications for the Earth System Model Evaluation and Development, J. Geophys. Res.-Atmos., 127, e2022JD036480, https://doi.org/10.1029/2022JD036480, 2022.

Chen, J., Liu, Y., Zhang, M., and Peng, Y.: Height Dependency of Aerosol-Cloud Interaction Regimes, J. Geophys. Res.-Atmos., 123, 491-506, https://doi.org/10.1002/2017JD027431, 2018.

Chen, S., Yau, M. K., and Bartello, P.: Turbulence Effects of Collision Efficiency and Broadening of Droplet Size Distribution in Cumulus Clouds, J. Atmos. Sci., 75, 203-217, https://doi.org/10.1175/JAS-D-17-0123.1, 2018.

Chen, Y. C., Xue, L., Lebo, Z. J., Wang, H., Rasmussen, R. M., and Seinfeld, J. H.: A comprehensive numerical study of aerosol-cloud-precipitation interactions in marine stratocumulus, Atmos. Chem. Phys., 11, 9749-9769, 10.5194/acp-11-9749-2011, 2011.

Christensen, M. W., Ma, P. L., Wu, P., Varble, A. C., Mülmenstädt, J., and Fast, J. D.: Evaluation of aerosol–cloud interactions in E3SM using a Lagrangian framework, Atmos. Chem. Phys., 23, 2789-2812, 10.5194/acp-23-2789-2023, 2023.

Comstock, K. K., Wood, R., Yuter, S. E., and Bretherton, C. S.: Reflectivity and rain rate in and below drizzling stratocumulus, Q. J. R. Meteor. Soc., 130, 2891-2918, https://doi.org/10.1256/qj.03.187, 2004.

Cooper, W. A., Friesen, R. B., Hayman, M., Jensen, J., Lenschow, D. H., Romashkin, P., Schanot, A., Spuler, S., Stith, J., and Wolff, C.: Characterization of Uncertainty in Measurements of Wind from the NSF/NCAR Gulfstream V Research Aircraft (No. NCAR/TN-528+STR), NCAR Technical Notes, doi:10.5065/D60G3HJ8, 2016.

Covert, D. S., Kapustin, V. N., Bates, T. S., and Quinn, P. K.: Physical properties of marine boundary layer aerosol particles of the mid-Pacific in relation to sources and meteorological transport, J. Geophys. Res.-Atmos., 101, 6919-6930, https://doi.org/10.1029/95JD03068, 1996.

D'Alessandro, J. J., McFarquhar, G. M., Wu, W., Stith, J. L., Jensen, J. B., and Rauber, R. M.: Characterizing the Occurrence and Spatial Heterogeneity of Liquid, Ice, and Mixed Phase Low-Level Clouds Over the Southern Ocean Using in Situ Observations Acquired During SOCRATES, J. Geophys. Res.-Atmos., 126, e2020JD034482, https://doi.org/10.1029/2020JD034482, 2021.

Danker, J., Sourdeval, O., McCoy, I. L., Wood, R., and Possner, A.: Exploring relations between cloud morphology, cloud phase, and cloud radiative properties in Southern Ocean's stratocumulus clouds, Atmos. Chem. Phys., 22, 10247-10265, 10.5194/acp-22-10247-2022, 2022.

Desai, N., Liu, Y., Glienke, S., Shaw, R. A., Lu, C., Wang, J., and Gao, S.: Vertical Variation of Turbulent Entrainment Mixing Processes in Marine Stratocumulus Clouds Using High-Resolution Digital Holography, J. Geophys. Res.-Atmos., 126, e2020JD033527, https://doi.org/10.1029/2020JD033527, 2021.

1209 Dong, X., Schwantes, A. C., Xi, B., and Wu, P.: Investigation of the marine boundary layer cloud and

1210   CCN properties under coupled and decoupled conditions over the Azores, J. Geophys. Res.-Atmos.,

1211   120, 6179-6191, https://doi.org/10.1002/2014JD022939, 2015.

1212 Dong, X., X. Zheng, B. Xi, and S. Xie (2023), A Climatology of Midlatitude Maritime Cloud Fraction and

1213   Radiative Effect Derived from the ARM ENA Ground-Based Observations, *J. Climate*, *36*(2), 531-546,

1214   doi:10.1175/JCLI-D-22-0290.1.

1215 Duong, H. T., Sorooshian, A., and Feingold, G.: Investigating potential biases in observed and modeled

1216   metrics of aerosol-cloud-precipitation interactions, Atmos. Chem. Phys., 11, 4027-4037,

1217   10.5194/acp-11-4027-2011, 2011.

1218 Fan, C., Wang, M., Rosenfeld, D., Zhu, Y., Liu, J., and Chen, B.: Strong Precipitation Suppression by

1219   Aerosols in Marine Low Clouds, Geophys. Res. Lett., 47, e2019GL086207,

1220   https://doi.org/10.1029/2019GL086207, 2020.

1221 Feingold, G., Frisch, A. S., Stevens, B., and Cotton, W. R.: On the relationship among cloud turbulence,

1222   droplet formation and drizzle as viewed by Doppler radar, microwave radiometer and lidar, J.

1223   Geophys. Res.-Atmos., 104, 22195-22203, https://doi.org/10.1029/1999JD900482, 1999.

1224 Feingold, G., Kreidenweis, S. M., Stevens, B., and Cotton, W. R.: Numerical simulations of

1225   stratocumulus processing of cloud condensation nuclei through collision-coalescence, J. Geophys.

1226   Res.-Atmos., 101, 21391-21402, https://doi.org/10.1029/96JD01552, 1996.

1227 Feingold, G. and McComiskey, A.: ARM's Aerosol–Cloud–Precipitation Research (Aerosol Indirect Effects),

1228   Meteor. Monogr., 57, 22.21-22.15, 10.1175/AMSMONOGRAPHS-D-15-0022.1, 2016.

1229 Feingold, G. and Siebert, H.: Cloud – Aerosol Interactions from the Micro to the Cloud Scale, from the

1230   Strungmann Forum Report, Clouds in the Perturbed Climate System: Their Relationship to Energy

1231   Balance, Atmospheric Dynamics, and Precipitation, 2, edited by: Heintzenberg, J. and Charlson, R.

1232   J., MIT Press, ISBN 978-0-262-01287-4, 2009.

Flossmann, A. I., Hall, W. D., and Pruppacher, H. R.: A Theoretical Study of the Wet Removal of Atmospheric Pollutants. Part I: The Redistribution of Aerosol Particles Captured through Nucleation and Impaction Scavenging by Growing Cloud Drops, J. Atmos. Sci., 42, 583-606, https://doi.org/10.1175/1520-0469(1985)042<0583:ATSOTW>2.0.CO;2, 1985.

Gao, S., Lu, C., Liu, Y., Mei, F., Wang, J., Zhu, L., and Yan, S.: Contrasting Scale Dependence of Entrainment-Mixing Mechanisms in Stratocumulus Clouds, Geophys. Res. Lett., 47, e2020GL086970, https://doi.org/10.1029/2020GL086970, 2020.

Ghate, V. P. and Cadeddu, M. P.: Drizzle and Turbulence Below Closed Cellular Marine Stratocumulus Clouds, J. Geophys. Res.-Atmos., 124, 5724-5737, https://doi.org/10.1029/2018JD030141, 2019.

Ghate, V. P., Cadeddu, M. P., Zheng, X., and O'Connor, E.: Turbulence in the Marine Boundary Layer and Air Motions below Stratocumulus Clouds at the ARM Eastern North Atlantic Site, J. Appl. Meteorol. Clim., 60, 1495-1510, 10.1175/JAMC-D-21-0087.1, 2021.

Grabowski, W. W. and Wang, L.-P.: Growth of Cloud Droplets in a Turbulent Environment, Annual Review of Fluid Mechanics, 45, 293-324, 10.1146/annurev-fluid-011212-140750, 2013.

Grosvenor, D. P., Sourdeval, O., Zuidema, P., Ackerman, A., Alexandrov, M. D., Bennartz, R., Boers, R., Cairns, B., Chiu, J. C., Christensen, M., Deneke, H., Diamond, M., Feingold, G., Fridlind, A., Hünerbein, A., Knist, C., Kollias, P., Marshak, A., McCoy, D., Merk, D., Painemal, D., Rausch, J., Rosenfeld, D., Russchenberg, H., Seifert, P., Sinclair, K., Stier, P., van Diedenhoven, B., Wendisch, M., Werner, F., Wood, R., Zhang, Z., and Quaas, J.: Remote Sensing of Droplet Number Concentration in Warm Clouds: A Review of the Current State of Knowledge and Perspectives, Reviews of Geophysics, 56, 409-453, https://doi.org/10.1029/2017RG000593, 2018.

Gupta, S., McFarquhar, G. M., O'Brien, J. R., Delene, D. J., Poellot, M. R., Dobracki, A., Podolske, J. R., Redemann, J., LeBlanc, S. E., Segal-Rozenhaimer, M., and Pistone, K.: Impact of the variability in vertical separation between biomass burning aerosols and marine stratocumulus on cloud

microphysical properties over the Southeast Atlantic, Atmos. Chem. Phys., 21, 4615– 4635, https://doi.org/10.5194/acp-21-4615-2021, 2021.

Gupta, S., McFarquhar, G. M., O'Brien, J. R., Poellot, M. R., Delene, D. J., Miller, R. M., and Small Griswold, J. D.: Factors affecting precipitation formation and precipitation susceptibility of marine stratocumulus with variable above- and below-cloud aerosol concentrations over the Southeast Atlantic, Atmos. Chem. Phys., 22, 2769–2793, https://doi.org/10.5194/acp-22-2769-2022, 2022.

Hansen, J. E. and Travis, L. D.: Light scattering in planetary atmospheres, Space Sci. Rev., 16, 527-610, doi:10.1007/BF00168069,1974.

Hill, A. A., Feingold, G., and Jiang, H.: The Influence of Entrainment and Mixing Assumption on Aerosol–Cloud Interactions in Marine Stratocumulus, J. Atmos. Sci., 66, 1450-1464, 10.1175/2008JAS2909.1, 2009.

Hinds, W.C.: Aerosol Technology, Properties, Behaviour, and Measurement of Airborne Particles. John Wiley & Sons Inc., New York., 1999.

Hoffmann, F. and Feingold, G.: A Note on Aerosol Processing by Droplet Collision-Coalescence, Geophys. Res. Lett., 50, e2023GL103716, https://doi.org/10.1029/2023GL103716, 2023.

Hu, A. Z., Igel, A. L., Chuang, P. Y., and Witte, M. K.: Recognition of Inter-Cloud Versus Intra-Cloud Controls on Droplet Dispersion With Applications to Microphysics Parameterization, J. Geophys. Res.-Atmos., 126, e2021JD035180, https://doi.org/10.1029/2021JD035180, 2021.

Hudson, J. G. and Noble, S.: CCN Spectral Shape and Cumulus Cloud and Drizzle Microphysics, J. Geophys. Res.-Atmos., 125, e2019JD031141, https://doi.org/10.1029/2019JD031141, 2020.

Jensen, M. P., Ghate, V. P., Wang, D., Apoznanski, D. K., Bartholomew, M. J., Giangrande, S. E., Johnson, K. L., and Thieman, M. M.: Contrasting characteristics of open- and closed-cellular stratocumulus cloud in the eastern North Atlantic, Atmos. Chem. Phys., 21, 14557-14571, 10.5194/acp-21-14557-2021, 2021.

Jones, C. R., Bretherton, C. S., and Leon, D.: Coupled vs. decoupled boundary layers in VOCALS-REx, Atmos. Chem. Phys., 11, 7143-7153, 10.5194/acp-11-7143-2011, 2011.

Jung, E., Albrecht, B. A., Sorooshian, A., Zuidema, P., and Jonsson, H. H.: Precipitation susceptibility in marine stratocumulus and shallow cumulus from airborne measurements, Atmos. Chem. Phys., 16, 11395-11413, 10.5194/acp-16-11395-2016, 2016.

Kang, L., Marchand, R. T., Wood, R., and McCoy, I. L.: Coalescence Scavenging Drives Droplet Number Concentration in Southern Ocean Low Clouds, Geophys. Res. Lett., 49, e2022GL097819, https://doi.org/10.1029/2022GL097819, 2022.

Kang, L., Marchand, R. T., and Wood, R.: Stratocumulus Precipitation Properties Over the Southern Ocean Observed From Aircraft During the SOCRATES Campaign, J. Geophys. Res.-Atmos., 129, e2023JD039831, https://doi.org/10.1029/2023JD039831, 2024.

Kim, S. H., Kim, J., Kim, J. H., and Chun, H. Y.: Characteristics of the derived energy dissipation rate using the 1 Hz commercial aircraft quick access recorder (QAR) data, Atmos. Meas. Tech., 15, 2277-2298, 10.5194/amt-15-2277-2022, 2022.

Lang, F., Ackermann, L., Huang, Y., Truong, S. C. H., Siems, S. T., and Manton, M. J.: A climatology of open and closed mesoscale cellular convection over the Southern Ocean derived from Himawari-8 observations, Atmos. Chem. Phys., 22, 2135-2152, 10.5194/acp-22-2135-2022, 2022.

Lu, C., Zhu, L., Liu, Y., Mei, F., Fast, J. D., Pekour, M. S., Luo, S., Xu, X., He, X., Li, J., and Gao, S.: Observational study of relationships between entrainment rate, homogeneity of mixing, and cloud droplet relative dispersion, Atmos. Res., 293, 106900, https://doi.org/10.1016/j.atmosres.2023.106900, 2023.

Lu, M.-L., Sorooshian, A., Jonsson, H. H., Feingold, G., Flagan, R. C., and Seinfeld, J. H.: Marine stratocumulus aerosol-cloud relationships in the MASE-II experiment: Precipitation susceptibility in eastern Pacific marine stratocumulus, J. Geophys. Res.-Atmos., 114, https://doi.org/10.1029/2009JD012774, 2009.

Deleted: over

Deleted: from

Deleted: during

Deleted: campaign, ESS Open Archive.,

Deleted: 22541/essoar.169290579.91095731/v1, 2023.

43

Mann, J. A. L., Christine Chiu, J., Hogan, R. J., O'Connor, E. J., L'Ecuyer, T. S., Stein, T. H. M., and Jefferson, A.: Aerosol impacts on drizzle properties in warm clouds from ARM Mobile Facility maritime and continental deployments, J. Geophys. Res.-Atmos., 119, 4136-4148, https://doi.org/10.1002/2013JD021339, 2014.

Mechem, D. B., Wittman, C. S., Miller, M. A., Yuter, S. E., and de Szoeke, S. P.: Joint Synoptic and Cloud Variability over the Northeast Atlantic near the Azores, J. Appl. Meteorol. Clim., 57, 1273-1290, https://doi.org/10.1175/JAMC-D-17-0211.1, 2018.

McComiskey, A., Feingold, G., Frisch, A. S., Turner, D. D., Miller, M. A., Chiu, J. C., Min, Q., and Ogren, J. A.: An assessment of aerosol-cloud interactions in marine stratus clouds based on surface remote sensing, J. Geophys. Res.-Atmos., 114, https://doi.org/10.1029/2008JD011006, 2009.

McCoy, I. L., Wood, R., and Fletcher, J. K.: Identifying Meteorological Controls on Open and Closed Mesoscale Cellular Convection Associated with Marine Cold Air Outbreaks, J. Geophys. Res.-Atmos., 122, 11,678-611,702, https://doi.org/10.1002/2017JD027031, 2017.

McCoy, I. L., McCoy, D. T., Wood, R., Regayre, L., Watson-Parris, D., Grosvenor, D. P., Mulcahy, J. P., Hu, Y., Bender, F. A. M., Field, P. R., Carslaw, K. S., and Gordon, H.: The hemispheric contrast in cloud microphysical properties constrains aerosol forcing, P. Natl. Acad. Sci. USA, 117, 18998-19006, 10.1073/pnas.1922502117, 2020.

McCoy, I. L., Bretherton, C. S., Wood, R., Twohy, C. H., Gettelman, A., Bardeen, C. G., and Toohey, D. W.: Influences of Recent Particle Formation on Southern Ocean Aerosol Variability and Low Cloud Properties, J. Geophys. Res.-Atmos., 126, e2020JD033529, https://doi.org/10.1029/2020JD033529, 2021.

McFarquhar, G. M., Bretherton, C. S., Marchand, R., Protat, A., DeMott, P. J., Alexander, S. P., Roberts, G. C., Twohy, C. H., Toohey, D., Siems, S., Huang, Y., Wood, R., Rauber, R. M., Lasher-Trapp, S., Jensen, J., Stith, J. L., Mace, J., Um, J., Järvinen, E., Schnaiter, M., Gettelman, A., Sanchez, K. J., McCluskey, C. S., Russell, L. M., McCoy, I. L., Atlas, R. L., Bardeen, C. G., Moore, K. A., Hill,

44

1336   T. C. J., Humphries, R. S., Keywood, M. D., Ristovski, Z., Cravigan, L., Schofield, R., Fairall, C.,

1337   Mallet, M. D., Kreidenweis, S. M., Rainwater, B., D'Alessandro, J., Wang, Y., Wu, W., Saliba, G.,

1338   Levin, E. J. T., Ding, S., Lang, F., Truong, S. C. H., Wolff, C., Haggerty, J., Harvey, M. J.,

1339   Klekociuk, A. R., and McDonald, A.: Observations of Clouds, Aerosols, Precipitation, and Surface

1340   Radiation over the Southern Ocean: An Overview of CAPRICORN, MARCUS, MICRE, and

1341   SOCRATES, B. Am. Meteorol. Soc., 102, E894-E928, https://doi.org/10.1175/BAMS-D-20-

1342   0132.1, 2021.

1343   Muñoz-Esparza, D., Sharman, R. D., and Lundquist, J. K.: Turbulence Dissipation Rate in the

1344   Atmospheric Boundary Layer: Observations and WRF Mesoscale Modeling during the XPIA Field

1345   Campaign, Mon. Weather Rev., 146, 351-371, https://doi.org/10.1175/MWR-D-17-0186.1, 2018.

1346   Olfert, J. S., Kulkarni, P., and Wang, J.: Measuring aerosol size distributions with the fast integrated

1347   mobility   spectrometer,   Journal   of   Aerosol   Science,   39,   940-956,

1348   https://doi.org/10.1016/j.jaerosci.2008.06.005, 2008.

1349   Painemal, D. and Zuidema, P.: Assessment of MODIS cloud effective radius and optical thickness

1350   retrievals over the Southeast Pacific with VOCALS-REx in situ measurements, J. Geophys. Res.-

1351   Atmos., 116, https://doi.org/10.1029/2011JD016155, 2011.

1352   Painemal, D., Chang, F. L., Ferrare, R., Burton, S., Li, Z., Smith Jr, W. L., Minnis, P., Feng, Y., and

1353   Clayton, M.: Reducing uncertainties in satellite estimates of aerosol–cloud interactions over the

1354   subtropical ocean by integrating vertically resolved aerosol observations, Atmos. Chem. Phys., 20,

1355   7167-7177, 10.5194/acp-20-7167-2020, 2020.

1356   Painemal, D., Spangenberg, D., Smith Jr, W. L., Minnis, P., Cairns, B., Moore, R. H., Crosbie, E.,

1357   Robinson, C., Thornhill, K. L., Winstead, E. L., and Ziemba, L.: Evaluation of satellite retrievals of

1358   liquid clouds from the GOES-13 imager and MODIS over the midlatitude North Atlantic during the

1359   NAAMES campaign, Atmos. Meas. Tech., 14, 6633-6646, 10.5194/amt-14-6633-2021, 2021.

Pinsky, M. B. and Khain, A. P.: Turbulence effects on droplet growth and size distribution in clouds—A review, Journal of Aerosol Science, 28, 1177-1214, https://doi.org/10.1016/S0021-8502(97)00005-0, 1997.

Pruppacher, H. R. and Klett, J. D.: Microphysics of clouds and precipitation, Kluwer Academic Publishers, Dordrecht, the Netherlands, 1997.

Rémillard, J. and Tselioudis, G.: Cloud Regime Variability over the Azores and Its Application to Climate Model Evaluation, J. Climate, 28, 9707-9720, https://doi.org/10.1175/JCLI-D-15-0066.1, 2015.

Sanchez, K. J., Roberts, G. C., Diao, M., and Russell, L. M.: Measured Constraints on Cloud Top Entrainment to Reduce Uncertainty of Nonprecipitating Stratocumulus Shortwave Radiative Forcing in the Southern Ocean, Geophys. Res. Lett., 47, e2020GL090513, https://doi.org/10.1029/2020GL090513, 2020.

Sanchez, K. J., Roberts, G. C., Saliba, G., Russell, L. M., Twohy, C., Reeves, J. M., Humphries, R. S., Keywood, M. D., Ward, J. P., and McRobert, I. M.: Measurement report: Cloud processes and the transport of biological emissions affect southern ocean particle and cloud condensation nuclei concentrations, Atmos. Chem. Phys., 21, 3427-3446, 10.5194/acp-21-3427-2021, 2021.

Stevens, B. and Feingold, G.: Untangling aerosol effects on clouds and precipitation in a buffered system, Nature, 461, 607-613, 10.1038/nature08281, 2009.

Siebert, H., Shaw, R. A., and Warhaft, Z.: Statistics of Small-Scale Velocity Fluctuations and Internal Intermittency in Marine Stratocumulus Clouds, J. Atmos. Sci., 67, 262-273, https://doi.org/10.1175/2009JAS3200.1, 2010.

Sorooshian, A., Feingold, G., Lebsock, M. D., Jiang, H., and Stephens, G. L.: On the precipitation susceptibility of clouds to aerosol perturbations, Geophys. Res. Lett., 36, https://doi.org/10.1029/2009GL038993, 2009.

1384 Terai, C. R. and Wood, R.: Aircraft observations of cold pools under marine stratocumulus, Atmos.
1385   Chem. Phys., 13, 9899-9914, 10.5194/acp-13-9899-2013, 2013.

1386 Terai, C. R., Wood, R., Leon, D. C., and Zuidema, P.: Does precipitation susceptibility vary with
1387   increasing cloud thickness in marine stratocumulus?, Atmos. Chem. Phys., 12, 4567-4583,
1388   10.5194/acp-12-4567-2012, 2012.

1389 Twohy, C. H., Petters, M. D., Snider, J. R., Stevens, B., Tahnk, W., Wetzel, M., Russell, L., and Burnet,
1390   F.: Evaluation of the aerosol indirect effect in marine stratocumulus clouds: Droplet number, size,
1391   liquid   water   path,   and   radiative   impact,   J.   Geophys.   Res.-Atmos.,   110,
1392   https://doi.org/10.1029/2004JD005116, 2005.

1393 vanZanten, M. C., Stevens, B., Vali, G., and Lenschow, D. H.: Observations of Drizzle in Nocturnal
1394   Marine Stratocumulus, J. Atmos. Sci., 62, 88-106, https://doi.org/10.1175/JAS-3355.1, 2005.

1395 Wacławczyk, M., Ma, Y. F., Kopeć, J. M., and Malinowski, S. P.: Novel approaches to estimating the
1396   turbulent kinetic energy dissipation rate from low- and moderate-resolution velocity fluctuation
1397   time series, Atmos. Meas. Tech., 10, 4573-4585, 10.5194/amt-10-4573-2017, 2017.

1398 Wang, J., Wood, R., Jensen, M. P., Chiu, J. C., Liu, Y., Lamer, K., Desai, N., Giangrande, S. E., Knopf,
1399   D. A., Kollias, P., Laskin, A., Liu, X., Lu, C., Mechem, D., Mei, F., Starzec, M., Tomlinson, J.,
1400   Wang, Y., Yum, S. S., Zheng, G., Aiken, A. C., Azevedo, E. B., Blanchard, Y., China, S., Dong,
1401   X., Gallo, F., Gao, S., Ghate, V. P., Glienke, S., Goldberger, L., Hardin, J. C., Kuang, C., Luke, E.
1402   P., Matthews, A. A., Miller, M. A., Moffet, R., Pekour, M., Schmid, B., Sedlacek, A. J., Shaw, R.
1403   A., Shilling, J. E., Sullivan, A., Suski, K., Veghte, D. P., Weber, R., Wyant, M., Yeom, J.,
1404   Zawadowicz, M., and Zhang, Z.: Aerosol and Cloud Experiments in the Eastern North Atlantic
1405   (ACE-ENA), B. Am. Meteorol. Soc., 103, E619-E641, 10.1175/BAMS-D-19-0220.1, 2022.

1406 Wang, Y., Zhao, C., McFarquhar, G. M., Wu, W., Reeves, M., and Li, J.: Dispersion of Droplet Size
1407   Distributions in Supercooled Non-precipitating Stratocumulus from Aircraft Observations Obtained

1408   during the Southern Ocean Cloud Radiation Aerosol Transport Experimental Study, J. Geophys.

1409   Res.-Atmos., 126, e2020JD033720, https://doi.org/10.1029/2020JD033720, 2021a.

1410 Wang, Y., Zheng, G., Jensen, M. P., Knopf, D. A., Laskin, A., Matthews, A. A., Mechem, D., Mei, F.,

1411   Moffet, R., Sedlacek, A. J., Shilling, J. E., Springston, S., Sullivan, A., Tomlinson, J., Veghte, D.,

1412   Weber, R., Wood, R., Zawadowicz, M. A., and Wang, J.: Vertical profiles of trace gas and aerosol

1413   properties over the eastern North Atlantic: variations with season and synoptic condition, Atmos.

1414   Chem. Phys., 21, 11079-11098, 10.5194/acp-21-11079-2021, 2021b.

1415 Wang, Y., Zheng, X., Dong, X., Xi, B., Wu, P., Logan, T., and Yung, Y. L.: Impacts of long-range

1416   transport of aerosols on marine-boundary-layer clouds in the eastern North Atlantic, Atmos. Chem.

1417   Phys., 20, 14741-14755, 10.5194/acp-20-14741-2020, 2020.

1418 Wang, Y., Zheng, X., Dong, X., Xi, B., and Yung, Y. L.: Insights of warm-cloud biases in Community

1419   Atmospheric Model 5 and 6 from the single-column modeling framework and Aerosol and Cloud

1420   Experiments in the Eastern North Atlantic (ACE-ENA) observations, Atmos. Chem. Phys., 23,

1421   8591-8605, 10.5194/acp-23-8591-2023, 2023.

1422 Wallace, J. M. and Hobbs, P. V.: Atmospheric Science: An Introductory Survey, 2nd edn., Academic

1423   Press/Elsevier, 483 pp, 2006.

1424 Witte, M. K., Chuang, P. Y., Ayala, O., Wang, L.-P., and Feingold, G.: Comparison of Observed and Simulated

1425   Drop Size Distributions from Large-Eddy Simulations with Bin Microphysics, Mon. Weather Rev., 147, 477-

1426   493, https://doi.org/10.1175/MWR-D-18-0242.1, 2019.

1427 Wood, R.: Drizzle in Stratiform Boundary Layer Clouds. Part I: Vertical and Horizontal Structure, J.

1428   Atmos. Sci., 62, 3011-3033, 10.1175/JAS3529.1, 2005.

1429 Wood, R.: Rate of loss of cloud droplets by coalescence in warm clouds, J. Geophys. Res.-Atmos., 111,

1430   https://doi.org/10.1029/2006JD007553, 2006.

1431 Wood, R., Wyant, M., Bretherton, C. S., Rémillard, J., Kollias, P., Fletcher, J., Stemmler, J., de Szoeke,

1432   S., Yuter, S., Miller, M., Mechem, D., Tselioudis, G., Chiu, J. C., Mann, J. A. L., O'Connor, E. J.,

Hogan, R. J., Dong, X., Miller, M., Ghate, V., Jefferson, A., Min, Q., Minnis, P., Palikonda, R., Albrecht, B., Luke, E., Hannay, C., and Lin, Y.: Clouds, Aerosols, and Precipitation in the Marine Boundary Layer: An Arm Mobile Facility Deployment, B. Am. Meteorol. Soc., 96, 419-440, 10.1175/BAMS-D-13-00180.1, 2015.

Wu, P., Dong, X., and Xi, B.: A Climatology of Marine Boundary Layer Cloud and Drizzle Properties Derived from Ground-Based Observations over the Azores, J. Climate, 33, 10133-10148, 10.1175/JCLI-D-20-0272.1, 2020.

Wu, P., Dong, X., Xi, B., Liu, Y., Thieman, M., and Minnis, P.: Effects of environment forcing on marine boundary layer cloud-drizzle processes, J. Geophys. Res.-Atmos., 122, 4463-4478, https://doi.org/10.1002/2016JD026326, 2017.

Wyant, M. C., Bretherton, C. S., Wood, R., Blossey, P. N., and McCoy, I. L.: High Free-Tropospheric Aitken-Mode Aerosol Concentrations Buffer Cloud Droplet Concentrations in Large-Eddy Simulations of Precipitating Stratocumulus, Journal of Advances in Modeling Earth Systems, 14, e2021MS002930, https://doi.org/10.1029/2021MS002930, 2022.

Yeom, J. M., Yum, S. S., Shaw, R. A., La, I., Wang, J., Lu, C., Liu, Y., Mei, F., Schmid, B., and Matthews, A.: Vertical Variations of Cloud Microphysical Relationships in Marine Stratocumulus Clouds Observed During the ACE-ENA Campaign, J. Geophys. Res.-Atmos., 126, e2021JD034700, https://doi.org/10.1029/2021JD034700, 2021.

Zawadowicz, M. A., Suski, K., Liu, J., Pekour, M., Fast, J., Mei, F., Sedlacek, A. J., Springston, S., Wang, Y., Zaveri, R. A., Wood, R., Wang, J., and Shilling, J. E.: Aircraft measurements of aerosol and trace gas chemistry in the eastern North Atlantic, Atmos. Chem. Phys., 21, 7983-8002, 10.5194/acp-21-7983-2021, 2021.

Zhang, J., Zhou, X., Goren, T., and Feingold, G.: Albedo susceptibility of northeastern Pacific stratocumulus: the role of covarying meteorological conditions, Atmos. Chem. Phys., 22, 861-880, 10.5194/acp-22-861-2022, 2022.

Zhang, X., Dong, X., Xi, B., and Zheng, X.: Aerosol Properties and Their Influences on Marine Boundary Layer Cloud Condensation Nuclei over the Southern Ocean, Atmosphere-Basel, 14, 10.3390/atmos14081246, 2023.

Zheng, G., Wang, Y., Aiken, A. C., Gallo, F., Jensen, M. P., Kollias, P., Kuang, C., Luke, E., Springston, S., Uin, J., Wood, R., and Wang, J.: Marine boundary layer aerosol in the eastern North Atlantic: seasonal variations and key controlling processes, Atmos. Chem. Phys., 18, 17615-17635, 10.5194/acp-18-17615-2018, 2018.

Zheng, G., Wang, Y., Wood, R., Jensen, M. P., Kuang, C., McCoy, I. L., Matthews, A., Mei, F., Tomlinson, J. M., Shilling, J. E., Zawadowicz, M. A., Crosbie, E., Moore, R., Ziemba, L., Andreae, M. O., and Wang, J.: New particle formation in the remote marine boundary layer, Nature Communications, 12, 527, 10.1038/s41467-020-20773-1, 2021.

Zheng, X., Dong, X., Ward, D. M., Xi, B., Wu, P., and Wang, Y.: Aerosol-Cloud-Precipitation Interactions in a Closed-cell and Non-homogenous MBL Stratocumulus Cloud, Adv. Atmos. Sci., 39, 2107-2123, 10.1007/s00376-022-2013-6, 2022a.

Zheng, X., Xi, B., Dong, X., Wu, P., Logan, T., and Wang, Y.: Environmental effects on aerosol–cloud interaction in non-precipitating marine boundary layer (MBL) clouds over the eastern North Atlantic, Atmos. Chem. Phys., 22, 335-354, 10.5194/acp-22-335-2022, 2022b.

Zuidema, P., Torri, G., Muller, C., and Chandra, A.: A Survey of Precipitation-Induced Atmospheric Cold Pools over Oceans and Their Interactions with the Larger-Scale Environment, Surveys in Geophysics, 38, 1283-1305, 10.1007/s10712-017-9447-x, 2017.
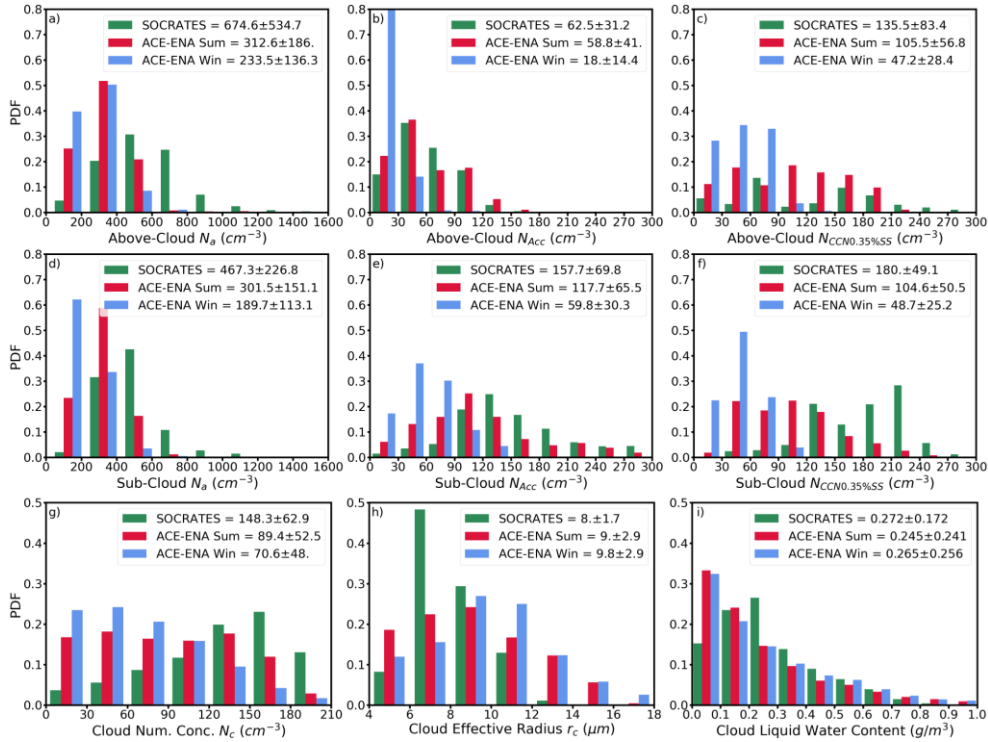
Figure 1. Probability Density Functions (PDFs) of N_a, N_{ACC} and $N_{CCN0.35\%}$ in the above-cloud (a, b, c) and sub-cloud (d, e, f) regimes; and the cloud microphysical properties of N_c (g), r_c (h), and LWC_c (f) within cloud layer. The statistical metrics in the legends denote the mean and standard deviation values for all samples in three IOPs. The ACE-ENA summer, winter and SOCRATES are color-coded with red, blue and green, respectively.
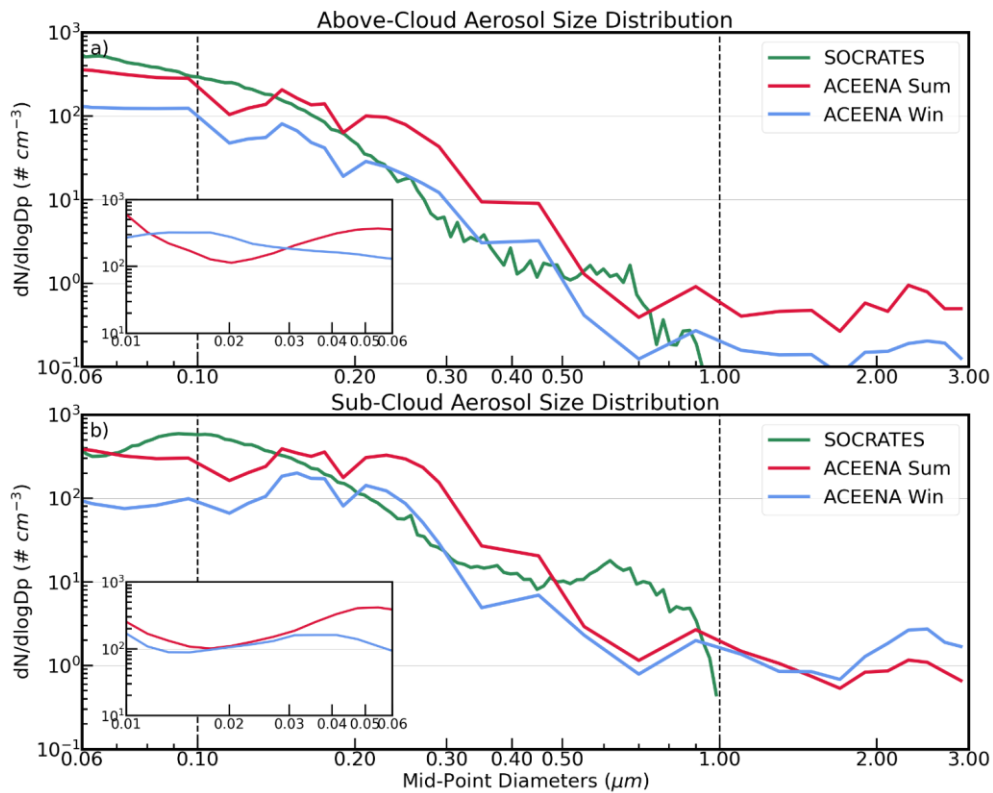
Figure 2. Aerosol size distributions ($D_p = 0.06 - 3$ µm) for above-cloud (a) and sub-cloud (b) regimes. The vertical dashed line at $D_p = 0.1$ µm and at $D_p = 1$ µm denotes the demarcations between Accumulation mode, Aitken mode and Coarse mode aerosols. The inner plots denote a smaller range of Aitken mode size distribution ($D_p = 0.01 - 0.06$ µm) available from ACE-ENA. The ACE-ENA summer, winter and SOCRATES are color-coded with red, blue and green, respectively.
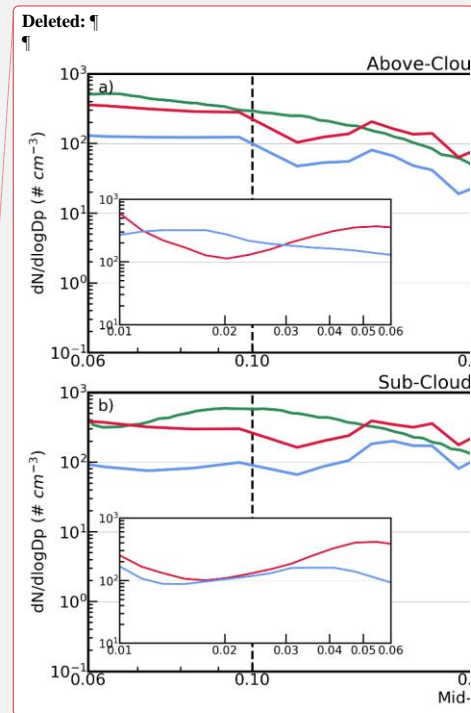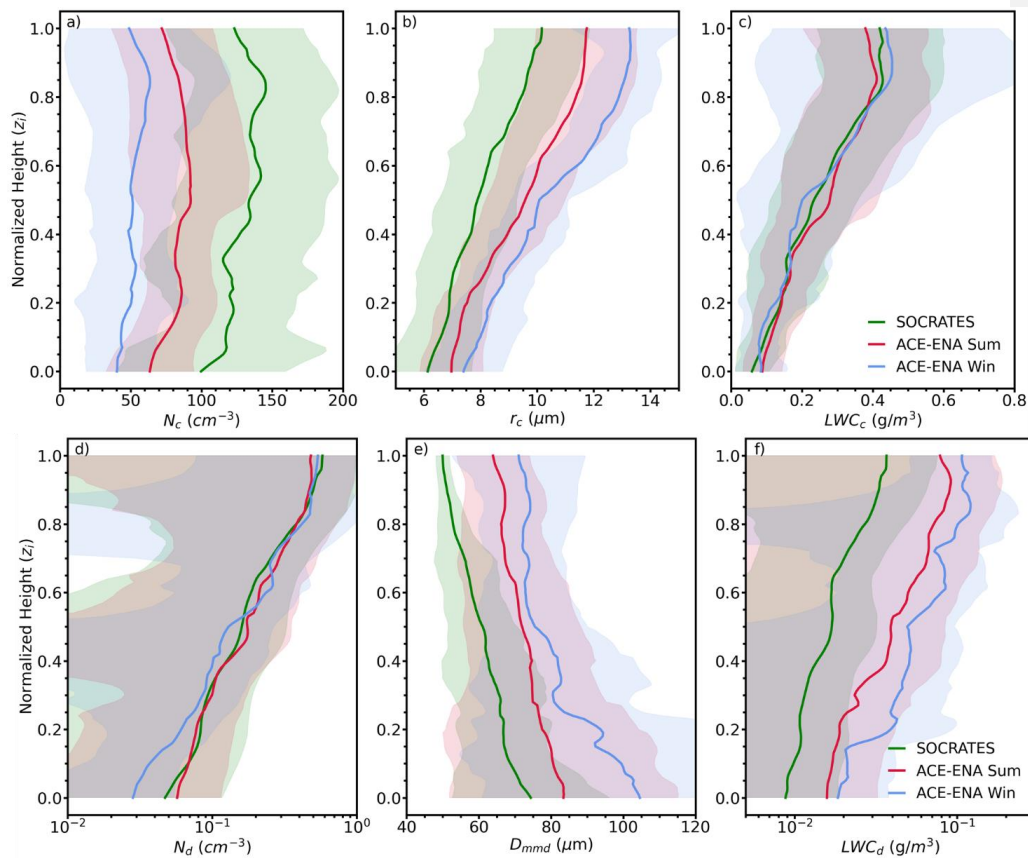
Figure 3. Vertical distributions of N_c (a), r_c (b), LWC_c (c), N_d (d), D_{mmd} (e), and LWC_d (f). Here the $z_i = 0$ denotes cloud base and $z_i = 1$ denotes cloud top. Shaded areas denote the inter-cloud-case standard deviations. The ACE-ENA summer, winter and SOCRATES are color-coded with red, blue and green, respectively.
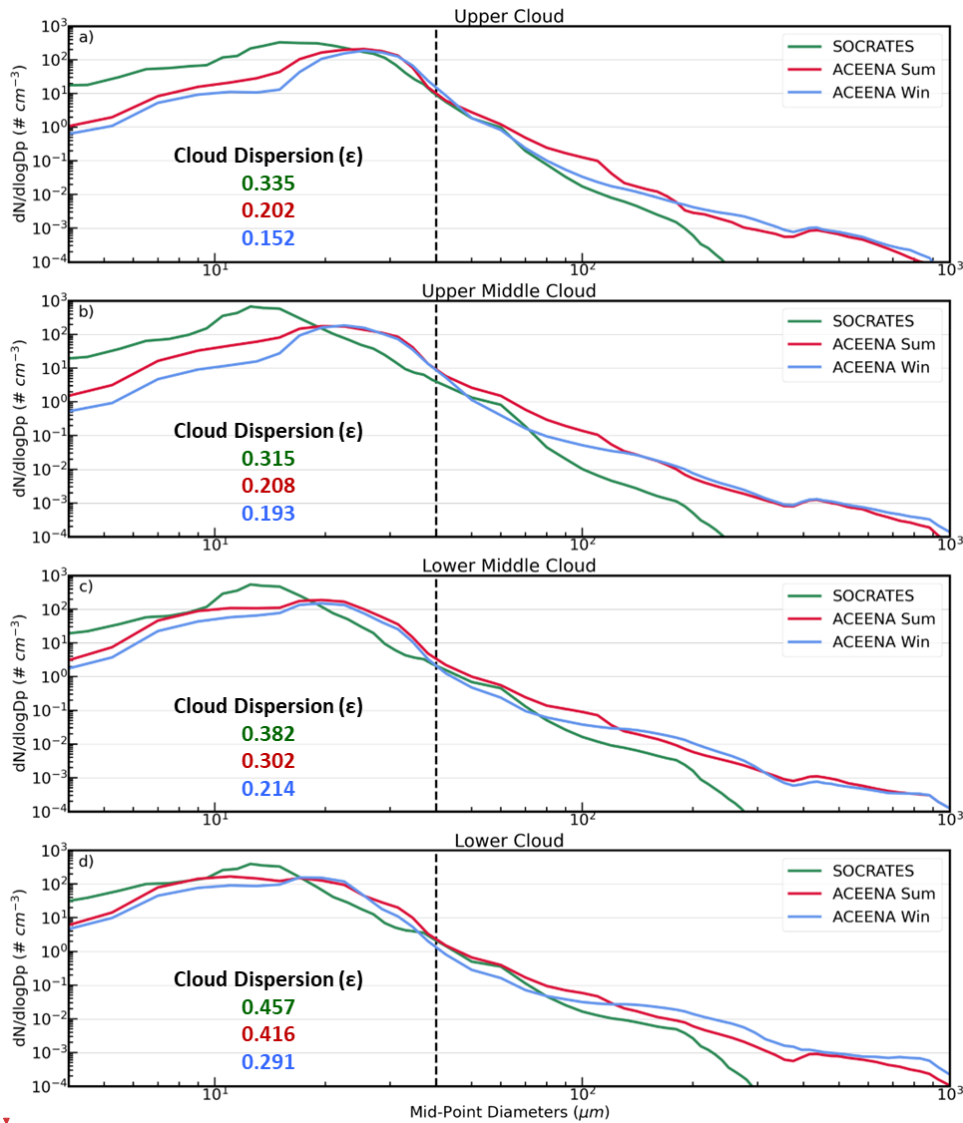
Figure 4. Cloud and drizzle size distributions for a) upper cloud ($z_i > 0.8$), b) upper-middle cloud ($0.5 \leq z_i < 0.8$), c) lower-middle cloud ($0.2 \leq z_i < 0.5$) and d) lower cloud ($z_i < 0.2$). The vertical dashed line at $D_p = 40$ µm denotes the demarcation between cloud droplets and drizzle drops. The ACE-ENA summer, winter and SOCRATES are color-coded with red, blue and green, respectively.
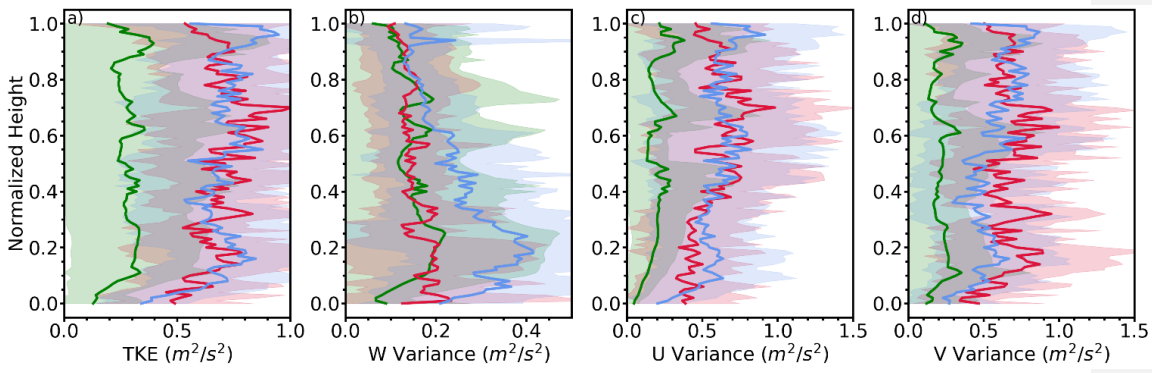
Figure 5. Vertical distributions of in-cloud TKE (a), w'^2 (b), u'^2 (c) and v'^2 (d). Shaded areas denote the inter-cloud-case standard deviations. The ACE-ENA summer, winter and SOCRATES are color-coded with red, blue and green, respectively.
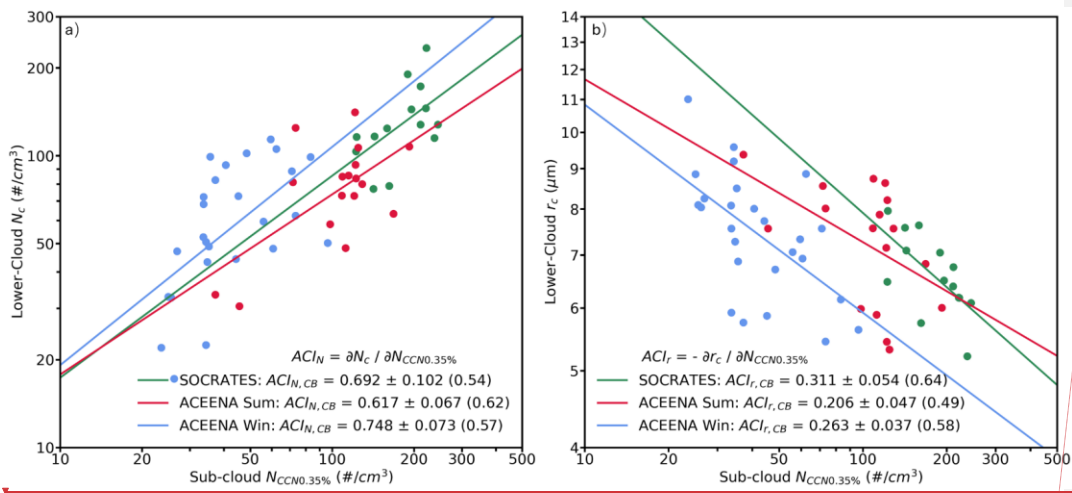
Figure 6. Scatterplots of the a) N_c and b) r_c at the lower-cloud ($z_i < 0.2$) against the sub-cloud $N_{CCN0.35\%}$. The statistical metrics in the legends denote the ACI values and standard errors, and the absolute values of correlation coefficients (in parentheses). The ACE-ENA summer, winter and SOCRATES are color-coded with red, blue and green, respectively.
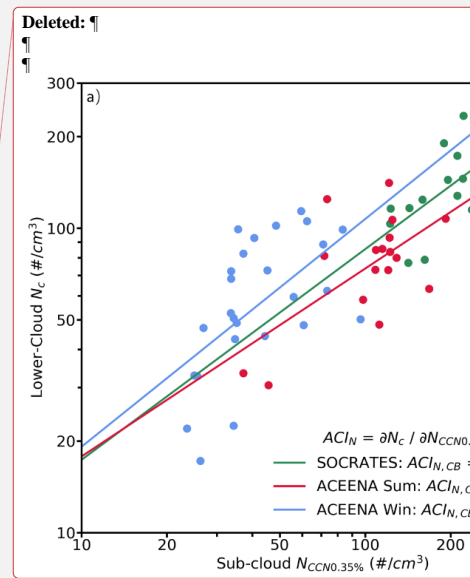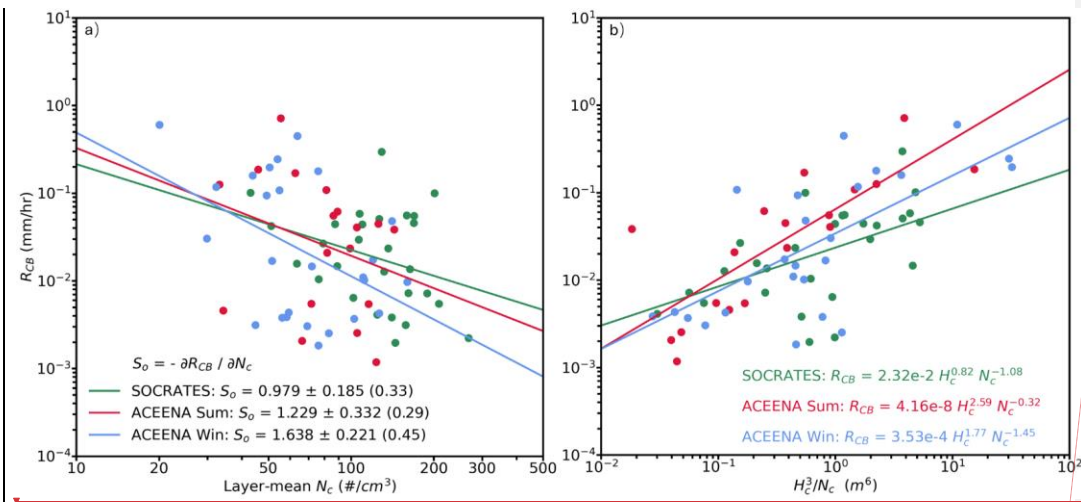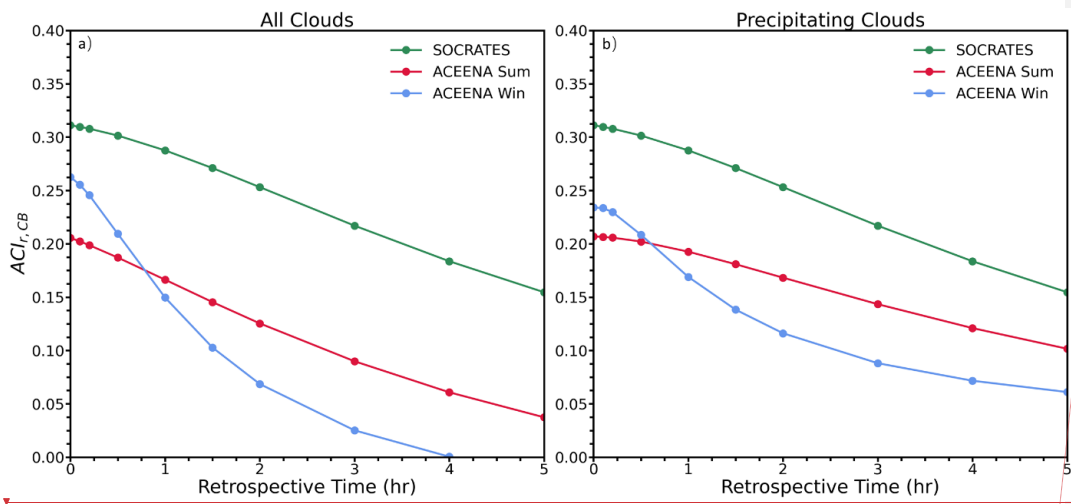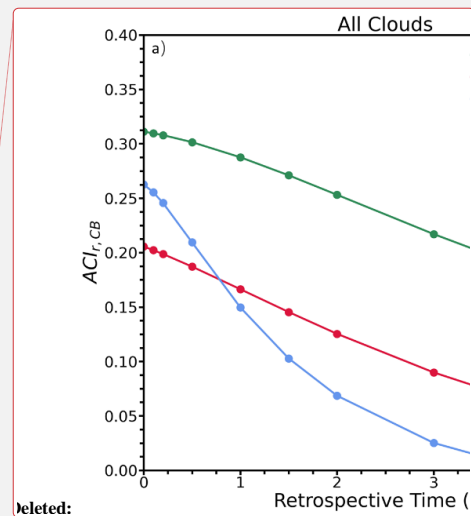
Figure 7. Scatterplots of the cloud base precipitation rate R_{CB} against the a) layer-mean N_c and b) H_c^3/N_c. ACE-ENA summer, winter and SOCRATES are color-coded with red, blue and green, respectively.
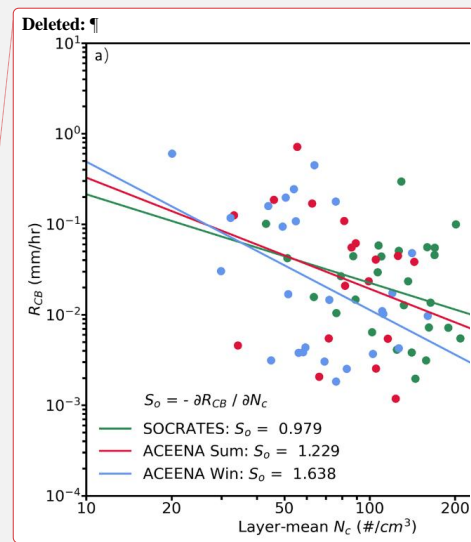
Figure 8. $ACI_{r,CB}$ as a function of the sub-cloud $N_{CCN0.35\%}$ retrospective time for a) all clouds and b) precipitating clouds.